Editors' Suggestion

# Dark Energy Survey Year 3: Blue shear

J. McCullough,[1,2,3,*] A. Amon,[1] E. Legnani,[4] D. Gruen,[5,6] A. Roodman,[3] O. Friedrich,[5] N. MacCrann,[7] M. Becker,[8] J. Myles,[1] S. Dodelson,[9,10] S. Samuroff,[11] J. Blazek,[11] J. Prat,[12,13] A. Pieres,[14,15] A. Ferté,[3] A. Alarcon,[8,16] A. Drlica-Wagner,[12,17,18] A. Choi,[19] A. Navarro-Alsina,[20] A. Campos,[21,10] A. A. Plazas Malagón,[22,3] A. Porredon,[23,24] A. J. Ross,[25] A. Carnero Rosell,[26,14] B. Yin,[21] B. Flaugher,[17] B. Yanny,[17] C. Sánchez,[27] C. Chang,[12,18] C. Davis,[22] C. To,[25] C. Doux,[27,28] D. Brooks,[29] D. J. James,[30] D. Sanchez Cid,[23] D. L. Hollowood,[31] D. Huterer,[32] E. S. Rykoff,[22,3] E. Gaztanaga,[33,34,16] E. M. Huff,[35] E. Suchyta,[36] E. Sheldon,[37] E. Sanchez,[23] F. Tarsitano,[38] F. Andrade-Oliveira,[32] F. J. Castander,[33,16] G. M. Bernstein,[27] G. Gutierrez,[17] G. Giannini,[39,18] G. Tarle,[32] H. T. Diehl,[17] H. Huang,[40,41] I. Harrison,[42] I. Sevilla-Noarbe,[23] I. Tutusaus,[43] I. Ferrero,[44] J. Elvin-Poole,[45] J. L. Marshall,[46] J. Muir,[47] J. Weller,[48,49] J. Zuntz,[50] J. Carretero,[39] J. DeRose,[51] J. Frieman,[17,18] J. Cordero,[52] J. De Vicente,[23] J. García-Bellido,[53] J. Mena-Fernández,[54] K. Eckert,[27] A. K. Romer,[55] K. Bechtol,[56] K. Herner,[17] K. Honscheid,[25,57] K. Kuehn,[58,59] L. F. Secco,[18] L. N. da Costa,[14] M. Paterno,[17] M. Soares-Santos,[32] M. Gatti,[27] M. Raveri,[60] M. Yamamoto,[61] M. Smith,[62] M. Carrasco Kind,[63,64] M. A. Troxel,[61] M. Jarvis,[27] M. E. C. Swanson,[63] N. Weaverdyck,[65,51] O. Lahav,[29] P. Doel,[29] P. Wiseman,[66] R. Miquel,[67,39] R. A. Gruendl,[63,64] R. Cawthon,[68] S. Allam,[17] S. R. Hinton,[69] S. L. Bridle,[52] S. Bocquet,[70] S. Desai,[71] S. Pandey,[27] S. Everett,[72] S. Lee,[35] T. Shin,[73] M. Aguena,[14] O. Alves,[32] E. Buckley-Geer,[12,17] D. L. Burke,[22,3] C. Conselice,[52,74] M. Crocce,[33,16] M. E. S. Pereira,[75] A. Farahi,[76,77] K. Honscheid,[25,57] N. Jeffrey,[29] M. Lima,[78,14] A. Palmese,[21] M. Schubnell,[32] V. Vikram,[8] M. Vincenzi,[79] and Y. Zhang[80]

(DES Collaboration)

[1]*Department of Astrophysical Sciences, Princeton University, Peyton Hall, Princeton, New Jersey 08544, USA*
[2]*Kavli Institute for Particle Astrophysics and Cosmology, Stanford University, Stanford, California 94305, USA*
[3]*SLAC National Accelerator Laboratory, Menlo Park, California 94025, USA*
[4]*Institut de Física d'Altes Energies (IFAE), The Barcelona Institute of Science and Technology, Campus UAB, 08193 Bellaterra Barcelona, Spain*
[5]*University Observatory, Faculty of Physics, Ludwig-Maximilians-Universität, Scheinerstrasse 1, 81679 Munich, Germany*
[6]*Excellence Cluster ORIGINS, Boltzmannstrasse 2, 85748 Garching, Germany*
[7]*Department of Applied Mathematics and Theoretical Physics, University of Cambridge, Cambridge CB3 0WA, United Kingodm*
[8]*Argonne National Laboratory, 9700 South Cass Avenue, Lemont, Illinois 60439, USA*
[9]*Department of Physics,Carnegie Mellon University, Pittsburgh, Pennsylvania 15312, USA*
[10]*NSF AI Planning Institute for Physics of the Future, Carnegie Mellon University, Pittsburgh, Pennsylvania 15213, USA*
[11]*Department of Physics, Northeastern University, Boston, Massachusetts 02115, USA*
[12]*Department of Astronomy and Astrophysics, University of Chicago, Chicago, Illinois 60637, USA*
[13]*Nordita, KTH Royal Institute of Technology and Stockholm University, Hannes Alfvéns väg 12, SE-10691 Stockholm, Sweden*
[14]*Laboratório Interinstitucional de e-Astronomia - LIneA, Rua Gal. José Cristino 77, Rio de Janeiro, RJ - 20921-400, Brazil*
[15]*Observatório Nacional, Rua Gal. José Cristino 77, Rio de Janeiro, RJ - 20921-400, Brazil*
[16]*Institute of Space Sciences (ICE, CSIC), Campus UAB, Carrer de Can Magrans, s/n, 08193 Barcelona, Spain*
[17]*Fermi National Accelerator Laboratory, P. O. Box 500, Batavia, Illinois 60510, USA*
[18]*Kavli Institute for Cosmological Physics, University of Chicago, Chicago, Illinois 60637, USA*
[19]*NASA Goddard Space Flight Center, 8800 Greenbelt Road, Greenbelt, Maryland 20771, USA*
[20]*Instituto de Física Gleb Wataghin, Universidade Estadual de Campinas, 13083-859, Campinas, SP, Brazil*
[21]*Department of Physics, Carnegie Mellon University, Pittsburgh, Pennsylvania 15312, USA*
[22]*Kavli Institute for Particle Astrophysics and Cosmology, P. O. Box 2450, Stanford University, Stanford, California 94305, USA*
[23]*Centro de Investigaciones Energéticas, Medioambientales y Tecnológicas (CIEMAT), Madrid, Spain*

 

[24]*Ruhr University Bochum, Faculty of Physics and Astronomy, Astronomical Institute, German Centre for Cosmological Lensing, 44780 Bochum, Germany*
[25]*Center for Cosmology and Astro-Particle Physics, The Ohio State University, Columbus, Ohio 43210, USA*
[26]*Instituto de Astrofisica de Canarias, E-38205 La Laguna, Tenerife, Spain*
[27]*Department of Physics and Astronomy, University of Pennsylvania, Philadelphia, Pennsylvania 19104, USA*
[28]*Université Grenoble Alpes, CNRS, LPSC-IN2P3, 38000 Grenoble, France*
[29]*Department of Physics and Astronomy, University College London, Gower Street, London, WC1E 6BT, United Kingdom*
[30]*Center for Astrophysics | Harvard & Smithsonian, 60 Garden Street, Cambridge, Massachusetts 02138, USA*
[31]*Santa Cruz Institute for Particle Physics, Santa Cruz, California 95064, USA*
[32]*Department of Physics, University of Michigan, Ann Arbor, Michigan 48109, USA*
[33]*Institut d'Estudis Espacials de Catalunya (IEEC), 08034 Barcelona, Spain*
[34]*Institute of Cosmology and Gravitation, University of Portsmouth, Portsmouth, PO1 3FX, United Kingdom*
[35]*Jet Propulsion Laboratory, California Institute of Technology, 4800 Oak Grove Dr., Pasadena, California 91109, USA*
[36]*Computer Science and Mathematics Division, Oak Ridge National Laboratory, Oak Ridge, Tennessee 37831*
[37]*Brookhaven National Laboratory, Bldg 510, Upton, New York 11973, USA*
[38]*Department of Physics, ETH Zurich, Wolfgang-Pauli-Strasse 16, CH-8093 Zurich, Switzerland*
[39]*Institut de Física d'Altes Energies (IFAE), The Barcelona Institute of Science and Technology, Campus UAB, 08193 Bellaterra (Barcelona) Spain*
[40]*Department of Astronomy/Steward Observatory, University of Arizona, 933 North Cherry Avenue, Tucson, Arizona 85721-0065, USA*
[41]*Department of Physics, University of Arizona, Tucson, Arizona 85721, USA*
[42]*School of Physics and Astronomy, Cardiff University, CF24 3AA, United Kingdom*
[43]*Institut de Recherche en Astrophysique et Planétologie (IRAP), Université de Toulouse, CNRS, UPS, CNES, 14 Av. Edouard Belin, 31400 Toulouse, France*
[44]*Institute of Theoretical Astrophysics, University of Oslo, P.O. Box 1029 Blindern, NO-0315 Oslo, Norway*
[45]*Department of Physics and Astronomy, University of Waterloo, 200 University Avenue W, Waterloo, Ontario N2L 3G1, Canada*
[46]*George P. and Cynthia Woods Mitchell Institute for Fundamental Physics and Astronomy, and Department of Physics and Astronomy, Texas A&M University, College Station, Texas 77843, USA*
[47]*Perimeter Institute for Theoretical Physics, 31 Caroline Street North, Waterloo, Ontario N2L 2Y5, Canada*
[48]*Max Planck Institute for Extraterrestrial Physics, Giessenbachstrasse, 85748 Garching, Germany*
[49]*Universitäts-Sternwarte, Fakultät für Physik, Ludwig-Maximilians Universität München, Scheinerstrasse 1, 81679 München, Germany*
[50]*Institute for Astronomy, University of Edinburgh, Edinburgh EH9 3HJ, United Kingdom*
[51]*Lawrence Berkeley National Laboratory, 1 Cyclotron Road, Berkeley, California 94720, USA*
[52]*Jodrell Bank Center for Astrophysics, School of Physics and Astronomy, University of Manchester, Oxford Road, Manchester, M13 9PL, United Kingdom*
[53]*Instituto de Fisica Teorica UAM/CSIC, Universidad Autonoma de Madrid, 28049 Madrid, Spain*
[54]*LPSC Grenoble - 53, Avenue des Martyrs 38026 Grenoble, France*
[55]*Department of Physics and Astronomy, Pevensey Building, University of Sussex, Brighton, BN1 9QH, United Kingdom*
[56]*Physics Department, 2320 Chamberlin Hall, University of Wisconsin-Madison, 1150 University Avenue Madison, Wisconsin 53706-1390*
[57]*Department of Physics, The Ohio State University, Columbus, Ohio 43210, USA*
[58]*Australian Astronomical Optics, Macquarie University, North Ryde, New South Wales 2113, Australia*
[59]*Lowell Observatory, 1400 Mars Hill Road, Flagstaff, Arizona 86001, USA*
[60]*Department of Physics, University of Genova and INFN, Via Dodecaneso 33, 16146, Genova, Italy*
[61]*Department of Physics, Duke University Durham, North Carolina 27708, USA*
[62]*Physics Department, Lancaster University, Lancaster, LA1 4YB, United Kingdom*
[63]*Center for Astrophysical Surveys, National Center for Supercomputing Applications, 1205 West Clark Street, Urbana, Illinois 61801, USA*

[64]Department of Astronomy, University of Illinois at Urbana-Champaign, 1002 W. Green Street, Urbana, Illinois 61801, USA
[65]Department of Astronomy, University of California, Berkeley, 501 Campbell Hall, Berkeley, California 94720, USA
[66]School of Physics and Astronomy, University of Southampton, Southampton, SO17 1BJ, United Kingdom
[67]Institució Catalana de Recerca i Estudis Avançats, E-08010 Barcelona, Spain
[68]Physics Department, William Jewell College, Liberty, Missouri 64068, USA
[69]School of Mathematics and Physics, University of Queensland, Brisbane, Queensland 4072, Australia
[70]University Observatory, Faculty of Physics, Ludwig-Maximilians-Universität, Scheinerstrasse 1, 81679 Munich, Germany
[71]Department of Physics, IIT Hyderabad, Kandi, Telangana 502285, India
[72]California Institute of Technology, 1200 East California Boulevard, MC 249-17, Pasadena, California 91125, USA
[73]Department of Physics and Astronomy, Stony Brook University, Stony Brook, New York 11794, USA
[74]University of Nottingham, School of Physics and Astronomy, Nottingham NG7 2RD, United Kingdom
[75]Hamburger Sternwarte, Universität Hamburg, Gojenbergsweg 112, 21029 Hamburg, Germany
[76]Departments of Statistics and Data Sciences, University of Texas at Austin, Austin, Texas 78757, USA
[77]NSF-Simons AI Institute for Cosmic Origins, University of Texas at Austin, Austin, Texas 78757, USA
[78]Departamento de Física Matemática, Instituto de Física, Universidade de São Paulo, CP 66318, São Paulo, SP, 05314-970, Brazil
[79]Department of Physics, University of Oxford, Denys Wilkinson Building, Keble Road, Oxford OX1 3RH, United Kingdom
[80]Cerro Tololo Inter-American Observatory, NSF's National Optical-Infrared Astronomy Research Laboratory, Casilla 603, La Serena, Chile

(Received 19 November 2024; accepted 17 February 2026; published 6 May 2026)

Modeling the intrinsic alignment (IA) of galaxies poses a challenge to weak lensing analyses. Using the Dark Energy Survey Year 3 shape catalog, we expect less impact from IA when we limit the sample to blue, star-forming galaxies. The cosmological parameter constraints from this BLUE cosmic shear sample are stable to IA model choice, unlike passive galaxies in the full DES Y3 sample, the goodness-of-fit is improved and the $\Omega_m$ and $S_8$ better agree with the observations from *Planck* on the cosmic microwave background. Mitigating IA with sample selection in DES, rather than flexible model choices, can reduce uncertainty in $S_8$ by a factor of 1.5.

DOI: 10.1103/wmp3-qc3p

## I. INTRODUCTION

Cosmic shear probes the growth of structures and the expansion of the Universe, providing a test of the standard cosmological model, $\Lambda$ cold dark matter ($\Lambda$CDM). It measures the tiny distortions of the apparent shapes of background galaxies due to the weak gravitational lensing by foreground large- scale structure. Over the last two decades, this technique has matured and produced high-precision measurements of the amplitude of the matter fluctuation spectrum, $S_8 = \sigma_8\sqrt{\Omega_m/0.3}$[1] [1–5]. These constraints all show a preference for $S_8$ to be lower than that expected according to the best fit $\Lambda$CDM cosmology derived from the cosmic microwave background *Planck* [6] (for a discussion see [7]).

Recent weak lensing surveys have demonstrated that their cosmological precision is limited by astrophysical systematic uncertainties [1,8]. Specifically, the dominant effects for cosmic shear are the modeling of the intrinsic alignment of galaxies (see [9,10] for a review) and baryon feedback (see, for example [11]). The Vera C. Rubin Observatory's Legacy Survey of Space and Time[2] (LSST), ESA's Euclid mission,[3] and Roman Space Telescope,[4] [12–14] are expected to lead to dramatic improvements in the statistical power of cosmic shear measurements. It is therefore critical to study these systematics to reduce their uncertainty and ensure that they do not bias cosmological inference [15].

*Contact author: jmccullough@princeton.edu

[1]Here $\sigma_8$ is the root mean square linear amplitude of the matter fluctuation spectrum in spheres of radius 8 $h^{-1}$ Mpc $h$ is the universal expansion rate in km s$^{-1}$ Mpc$^{-1}$ scaled by a factor of 1/100 and $\Omega_m$ is the present day matter density.

[2]https://www.lsst.org.
[3]https://www.euclid-ec.org.
[4]https://roman.gsfc.nasa.gov.

Modern cosmic shear analyses commonly model intrinsic alignments using the nonlinear alignment model [NLA; e.g., [16,17] ] and the Tidal Alignment and Tidal Torquing model [TATT; [18] ]. NLA describes the linear tidal alignment of galaxies with the density field [17], including an *ad hoc* nonlinear correction to the linear matter power spectrum [16], and a redshift dependence (NLA-$z$, [19]). TATT extends NLA with the inclusion of a tidal torquing alignment mechanism. Critically, beyond a cost in precision, this IA model choice impacts the value of the reported cosmological constraints by $\sim 0.5\sigma$ [1,5,8,20] because uncertain IA model parameters are degenerate with cosmological parameters. As progress is made to build flexible feedback models that allow for cosmic shear analyses to utilize the full angular scale extent of measurements, IA modeling, which is more uncertain at small scales, comes into focus. This highlights the importance to distinguish between IA models, or to devise new strategies to mitigate their impact.

The NLA and TATT models provide good fits to direct measurements of IA, which are constructed from weak lensing data that overlaps with accurate galaxy distances, such as spectroscopy [e.g., [21] ]. However, these measurements are limited to larger scales than cosmic shear analyses probe (6 Mpc$/h$ and $k \sim 1$ for NLA and 2 Mpc$/h$ and $k \sim 3$ for TATT). We note that even though TATT provides accuracy on smaller scales, it has been found that cosmic shear data has a mild preference for the simpler NLA model over TATT [5], though NLA breaks down from observation more quickly at smaller scales [22]. To make progress on our understanding of IA, there has been an effort to develop more sophisticated models based on the halo model [23] or other analytic approaches [e.g., [24–29] ], however many of these incur additional model parameters and exacerbate the precision cost [30]. Another avenue has been to test models in hydrodynamical simulations, but these show a range of IA scenarios [31,32].

It has been established from direct IA measurements that redder, elliptical galaxies at low redshift exhibit strong intrinsic alignment that is well described by NLA on large ($\gtrsim 10\ h^{-1}$ Mpc) scales [33,34], and that the strength of this alignment depends on galaxy luminosity [21,35]. Bluer, star-forming galaxies have not been found to have any intrinsic alignment—though direct measurements are limited [21,36,37]. Indeed, a limitation of the NLA model is that it treats spiral galaxies and ellipticals equally, despite the very different physical mechanisms by which tidal forces may affect their shapes [38,39]. Previously, cosmic shear data has been reanalyzed with separate IA model parameters for star-forming (blue) and elliptical (red) galaxies in order to study the color-dependence of IA [within DES with [40] ], with progenitors in other surveys [e.g., [41,42] ]. This analysis builds on this work but is driven by IA mitigation in order to realize cosmological posteriors that are stable to the IA model choice.

In this paper, to bridge the limitations of IA model choice, model inaccuracies on small scales and precision-loss due to uninformed model space, we test a new approach to account for intrinsic alignments through sample selection. We construct a high-purity sample of star-forming galaxies from the Dark Energy Survey (DES) Year 3 (Y3) lensing data, that *a priori* is expected to have no or minimal IA consistent with presently uncertain direct measurements, therefore circumventing the need for an IA model in the cosmic shear analysis [43]. We calibrate this data, measure the 2-point shear correlation functions and analyze them to demonstrate a cosmic shear cosmology result that is stable to the choice of IA model. Without the additional concern of an accurate model on small angular scales, we analyze the full measurements using a flexible model for baryon feedback. We examine the remaining mixed sample with a high fraction of passive, redder elliptical galaxies to test the IA model suitability. In Sec. II we present the methodology for selecting an IA-clean sample and summarize the subsequent shear measurement. In Sec. II B, we outline the model choices and framework. The main results of this paper are contained in Sec. III and we discuss the implications of our findings in Sec. IV.

## II. METHODOLOGY

This work expands upon the DES Y3 cosmic shear analysis [1,5]. DES Y3 weak lensing data spans 4143 deg$^2$ with $riz$ photometry and METACALIBRATION shapes [44] and is divided into four redshift bins [45]. For each redshift bin, we select a high-purity star-forming sample, BLUE, described in Sec. II A, leaving a predominantly elliptical sample, RED. We calibrate the redshift distributions of the data (Fig. 1) following the SOMPZ methodology, which hinges on deep fields with overlapping near-infrared observations [46] and survey characterization with BALROG [47], used in a self-organizing map (SOM) framework. We repeat the shear calibration for the BLUE and RED samples [48], which is based upon image simulations. This calibration and any customization of the DES Y3 strategy is described further in Appendix B. The selection, properties and calibration parameters of the sample are quantified in Table I. Measurements of the BLUE and RED shear 2-point functions are presented in Sec. II C.

### A. Selection of star-forming galaxies

For each of the four DES Y3 redshift bins [45], we select on $r-z$ color of a DES Y3 SOM cell, visualized in the inset panels in Fig. 1. As we do not have measurements of the intrinsic, rest-frame color for each galaxy, our observed color bound increases with each tomographic bin, accounting for the apparent reddening of these galaxies in the distant Universe. The selection is designed to maximize the

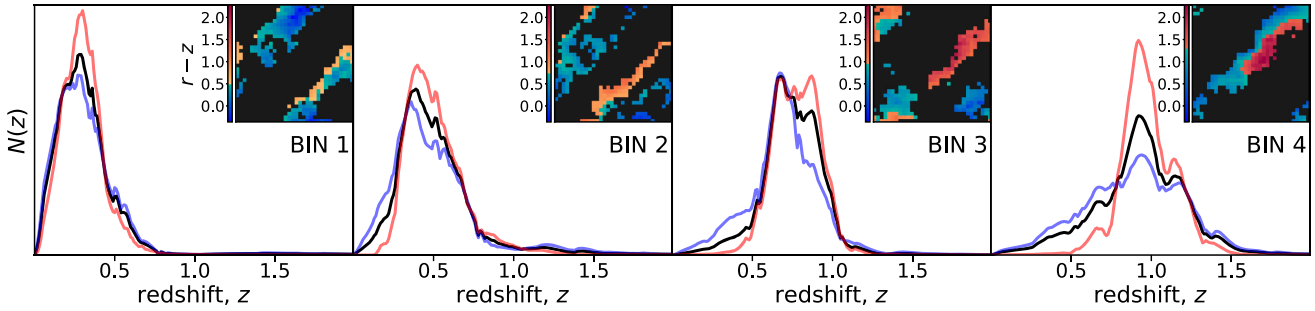


FIG. 1. The calibrated redshift distributions for the BLUE, RED, and FULL samples (black) for each DES Y3 redshift bin, where the SOM selection is shown in the insets (cells not selected for the redshift bin are filled in black).

purity of the BLUE sample and therefore minimize intrinsic alignment. While for the vast majority of galaxies we have only *riz* colors alongside their shapes, the deep-fields contain a wealth of information in $ugrizJHK_s$ photometry that can aid and characterize our fiducial selection. The selection is tuned to produce sufficient statistics for cosmic shear, and red galaxies are excluded with high fidelity using three cross-checks informed by deep field inference of passive galaxy fractions: (1) SED fitting with BAGPIPES [49], which models the emission from galaxies and allows us to select red galaxies with negligible star formation rates, (2) SED fitting with EAZY [50], which allows for selection on galaxies dominated by passive galaxy templates—complementary to BAGPIPES as the selection is on template coefficients and not derived galaxy properties, and (3) observed color in the filters bracketing the Balmer break at the inferred photometric redshift (for more detail, see Appendix A). The $r-z$ boundary that defines the BLUE sample, the fraction of the sample per bin and the purity estimated by each method is given in Table I. These indicate that the BLUE sample is $\lesssim$3% contaminated with red galaxies (as the Balmer break method overestimates the total red fraction), and comprises 65 percent of the Y3 sample. We note that even the RED sample is estimated to be only ∼20%–30% red.

Compared to previous work, our emphasis is on purity in the BLUE sample to derive an IA-clean sample, rather than have a well-defined red and blue split. Our sample selection is improved and better controlled, aided by the 8-band deep field information and the SOMPZ framework, without a reliance on BPZ templates compared to optical-only information.

### B. Cosmic shear modeling

The cosmic shear measurements, $\xi_\pm$, can be written as a function of a convergence $\kappa$ power spectrum, which results from the 3D nonlinear matter power spectrum computed at a given choice of cosmological parameters. For the modeling and analysis, we closely follow the DES Y3 choices [1,5], detailed in Appendix C with salient updates summarized as

(i) Following Ref. [8], we model the nonlinear power spectrum using HMCODE [51] and we account for baryon feedback by marginalizing over the $\log_{10} T_{\rm AGN}$ parameter. Following the model tests in Ref. [11], we choose a flexible prior of 7.6–8.3 to account for extreme feedback scenarios.

(ii) We analyze the full range of angular scales plotted in Fig. 2. The DES Y3 scale cuts (defined in [1,5]) are

TABLE I. The statistics of the BLUE and RED galaxy subsamples of the DES Y3 data for each redshift bin, including the effective number density $n_{\rm eff}$ (gal/arcmin$^2$), the average per-component shape noise, $\langle\sigma_e\rangle$, the calibrated mean redshift, $\langle z\rangle$, the uncertainty in the mean redshift (adopted from [45]), $\Delta z$, and the shear calibration parameter, $m$. For each bin, the subsamples are divided by the cell $r-z$ selection value, tuned and characterized by the fraction of passive, red galaxies inferred from the optical and near-infrared deep field data using three techniques (see Sec. II A).

| Bin | $r-z$ Selection | No. objects | Frac. of DES Y3 | $n_{\rm eff}$ | $\langle\sigma_e\rangle$ | $\langle z\rangle$ | % Red (BAGPIPES) | % Red (EAZY) | % Red (balmer) | $\Delta z$ | $m\times 100$ |
|---|---|---|---|---|---|---|---|---|---|---|---|
| BLUE, 1 | $<0.50$ | 18031829 | 0.725 | 1.054 | 0.255 | 0.3556 | 1.14 | 1.51 | 4.77 | 0.018 | $-1.29\pm0.91$ |
| BLUE, 2 | $<0.75$ | 16670470 | 0.660 | 0.988 | 0.282 | 0.5175 | 2.71 | 3.13 | 9.21 | 0.015 | $-1.80\pm0.78$ |
| BLUE, 3 | $<0.95$ | 12233530 | 0.493 | 0.726 | 0.275 | 0.6994 | 2.81 | 2.94 | 7.79 | 0.011 | $-2.03\pm0.76$ |
| BLUE, 4 | $<1.30$ | 18130765 | 0.718 | 1.073 | 0.325 | 0.8994 | 2.22 | 2.88 | 6.51 | 0.017 | $-3.56\pm0.76$ |
| RED, 1 | $>0.50$ | 6850889 | 0.275 | 0.439 | 0.227 | 0.3025 | 18.14 | 19.20 | 36.20 | 0.018 | $-0.89\pm0.91$ |
| RED, 2 | $>0.75$ | 8554173 | 0.340 | 0.548 | 0.246 | 0.5116 | 27.92 | 26.98 | 55.05 | 0.015 | $-1.78\pm0.78$ |
| RED, 3 | $>0.95$ | 12597837 | 0.507 | 0.780 | 0.242 | 0.7757 | 25.63 | 21.77 | 46.75 | 0.011 | $-2.37\pm0.76$ |
| RED, 4 | $>1.30$ | 7134533 | 0.282 | 0.418 | 0.294 | 0.9851 | 30.46 | 29.25 | 42.12 | 0.017 | $-3.15\pm0.76$ |

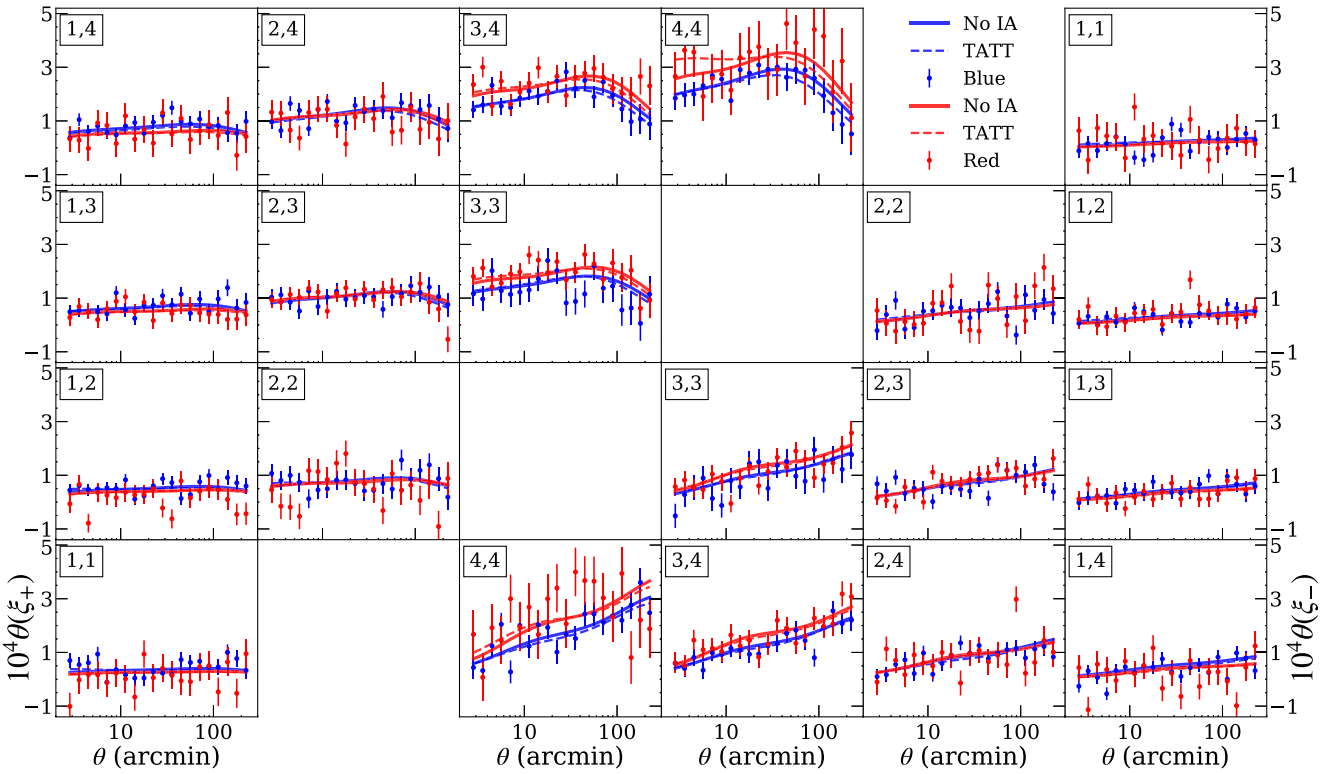


FIG. 2. Cosmic shear two-point correlation measurements for each redshift bin pair, $\xi_\pm$, for the BLUE and RED samples. The error bars represent the square root of the diagonal of the analytic covariance matrix. The solid lines represent the best model fit for ΛCDM with no intrinsic alignment, which is preferred by both selections, and the dashed lines represent the best fit for TATT, the most complex IA model choice considered. Notable shifts are at small scales in the autocorrelation for bin 4—marked [4,4]. For residuals, see Fig. 10.

primarily designed to mitigate the impact of baryon feedback, however, even with conservative feedback modeling, the fidelity of the NLA and TATT intrinsic alignment models on small-scales is uncertain. A key advantage of mitigating IA through sample selection with a BLUE sample demonstrated in this paper is the ability to safely exploit the small-scale cosmic shear measurements.

(iii) We assume three neutrino species with two massless states and one massive state and a mass of 0.06 eV, which has been shown to have a negligible impact [5,8,11].

Here we briefly describe the intrinsic alignments models. The observed ellipticity of a galaxy, $\epsilon_{\rm obs}$, can be approximately written as having linear contributions from cosmic shear, $\gamma_{\rm lens}$, the intrinsic alignment, $\gamma_{\rm IA}$ and its true shape, $\epsilon_{\rm no\ IA}$: $\epsilon_{\rm obs} \approx \epsilon_{\rm no\ IA} + \gamma_{\rm lens} + \gamma_{\rm IA}$. The orientation of $\epsilon_{\rm no\ IA}$ is uncorrelated between any two galaxies, but $\gamma_{\rm lens}$ and $\gamma_{\rm IA}$ are spatially coherent, and correlated with one another, for pairs of galaxies. Appendix C details how this propagates into our measurements as a function of galaxy pair separation.

The TATT IA model [18], which was the fiducial choice for the DES Y3 [1,5] and HSC Y3 [3,4] analyses, allows for more complexity than the NLA, favored in [e.g., [2,8] ]. Within TATT, the responses to large-scale tidal fields are encapsulated in three parameters: $A_1$, $A_2$, and $A_{1\delta}$. These correspond to a linear response of galaxy shape to the tidal field (tidal alignment), a quadratic response (tidal torquing), and a response to the product of the density and tidal fields (density weighting)

$$\gamma_{ij}^{IA} = A_{1\delta}(\delta \times s_{ij}) + A_1\, s_{ij} + A_2\left(\sum_{k=0}^{2} s_{ik}\, s_{kj} - \frac{1}{3}\delta_{ij} s^2\right), \quad (1)$$

where $\delta$ and $s$ describe the density and tidal fields, respectively. The redshift evolution of $A_1$ and $A_2$ is parametrized as a power law, governed by $\eta_1$ and $\eta_2$, and given by,

$$A_{1\delta}(z) = b_{\rm ta} A_1(z), \quad (2)$$

$$A_1(z) = -a_1 \bar{C}_1 \frac{\rho_{\rm m}}{D(z)} \left(\frac{1+z}{1+z_p}\right)^{\eta_1}, \quad (3)$$

$$A_2(z) = 5 a_2 \bar{C}_1 \frac{\rho_{\rm m}}{D(z)^2} \left(\frac{1+z}{1+z_p}\right)^{\eta_2}, \quad (4)$$

where $D(z)$ is the linear growth factor, $\rho_{\rm m} = \Omega_{\rm m}\rho_{\rm crit}$ is the matter density, $\bar{C}_1$ is a normalization constant by convention fixed at a value of $5 \times 10^{-14} M_\odot\ h^{-1}$ Mpc$^2$ [52], and $z_p$ is a pivot redshift, which we fix to the value 0.62 [53]. In the absence of informative priors, the analysis marginalizes

over all five IA parameters that govern the amplitude and redshift dependence of the signal, $(a_1, a_2, \eta_1, \eta_2, b_{\rm ta})$, with noninformative flat priors summarized in Appendix C. Other IA models are nested within the TATT framework, where the simplest, single parameter model corresponds to only $a_1$ being varied (NLA). Uncertainty or mismodeling of IA can also enter our analysis as shifts of the mean of the redshift distributions, discussed further in Appendix C 4.

### C. Cosmic shear measurements

We follow the DES Y3 methodology [1,5,54] to compute the cosmic shear measurements and covariance for the BLUE and RED samples. The shear two-point correlation function is determined by averaging over galaxy pairs, (1,2), separated by an angle, $\theta$, for two redshift bins, $(i, j)$, as

$$\xi^{ij}_{\pm}(\theta) = \frac{\sum_{1,2} w_1 w_2 [\epsilon^i_t \epsilon^j_t \pm \epsilon^i_\times \epsilon^j_\times]}{\sum_{1,2} R_a R_b w_1 w_2}, \tag{5}$$

in terms of their measured radial and tangential ellipticities, $\epsilon_\times$ and $\epsilon_t$, and where galaxy pairs are weighted by an inverse variance of the shear information they contain, $w$, and a metacalibration response, $R$, that corrects for biases due to sample selection and shear measurement [44]. The measurements are shown in Fig. 2 alongside their best-fit models using TATT and no IA model.[5]

## III. RESULTS AND DISCUSSION

We determine the posterior of cosmological and nuisance parameters by sampling the prior and likelihood function. The 2D marginalized constraints on the matter fluctuation amplitude $S_8$, and matter density $\Omega_{\rm m}$, for the BLUE sample are summarized in Fig. 3. The mean values of $S_8$ and their 68% credible intervals for three IA model variants are found to be

$$\begin{aligned} \text{no IA}: S_8 &= 0.822^{+0.019}_{-0.020} \\ \text{NLA}: \ S_8 &= 0.820^{+0.023}_{-0.024} \\ \text{TATT}: \ S_8 &= 0.793^{+0.044}_{-0.030}, \end{aligned} \tag{6}$$

which are consistent within $0.5\sigma$. Table II lists the constraints on $S_8$ and $\Omega_{\rm m}$ for all three samples. We compare our proposed no IA blue sample cosmic shear analysis to the results from the DES Y3 approach, which discarded small-scale measurements (ΛCDM-optimized scale cuts) to limit the impact of astrophysical systematics, primarily baryon feedback, and used the TATT IA model. This has the added value to minimizing the impact of IA, e.g., [1,5,8,53]. These fiducial choices are shown in Fig. 3 alongside the same scale-cuts with the popular NLA model. For reference, we compare to the CMB constraint from *Planck* TTTEEE[6] ΛCDM analysis [55]. Our approach to mitigate IA through a pure blue selection and a flexible baryon model allows for safe use of all angular scales of the measurement. It produces almost a factor of two improvement on the $S_8$ constraint, despite having lower statistical weight—due in part to the advantage of fewer model parameters. While the use of scale cuts on the FULL sample does reduce the slight disagreement in $\Omega_{\rm m}$ between the FULL and BLUE samples, the $S_8$ value falls below the BLUE result by $1.3\sigma$.

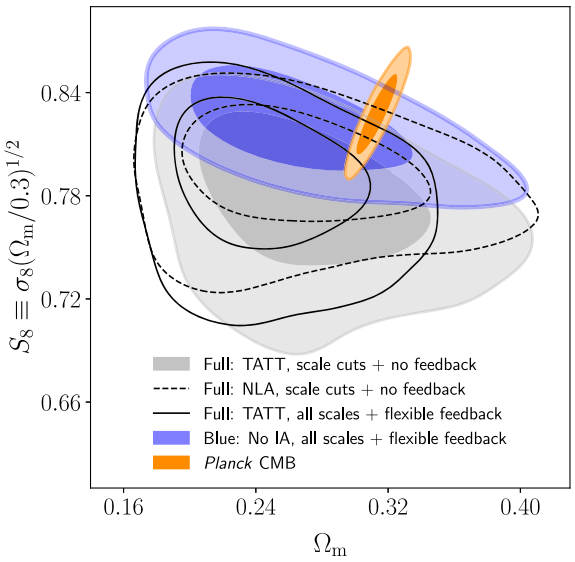


FIG. 3. Marginalized posteriors for $\Omega_{\rm m}$ and $S_8$ derived from cosmic shear measurements using only BLUE galaxies, designed to mitigate the effects of IA (blue). These are analyzed with a flexible baryon feedback model, and compared to the FULL DES Y3 sample using the same feedback model and the TATT IA model (black line), producing a lower value for $S_8$ and $\Omega_m$. We also compare to the Y3 approach to exclude small-scale measurements of FULL sample and model IA using TATT (gray filled) and NLA (black dashed). At a cost of removing 35% galaxies, the BLUE shear $S_8$ constraint is 1.5× improved precision and shifts $1.5\sigma$ higher. The *Planck* TTTEEE constraints are shown in orange [55].

In Fig. 4 we contrast the cosmological constraints derived from analyses of the BLUE and RED samples using three IA model variants: no IA model, NLA and TATT. The BLUE sample shows stability across IA model choices, whereas the $S_8$ values obtained for the RED in

[5]In the course of this work, we found the Y3 fiducial analysis was performed with an outdated tomographic binning. As a consequence of this, we created an updated full (unsplit by color) data vector. This update slightly improves the $\chi^2_{\rm min}$ and minutely changes the cosmic shear cosmology. The FULL sample in this analysis is not identical to the Y3 fiducial as a result; note the updated catalog binning in https://des.ncsa.illinois.edu/releases/y3a2/Y3key-catalogs.

[6]The high multipole likelihood attained from combining the temperature power spectra (TT), temperature-polarization E-mode cross spectra (TE) and polarization E-mode power spectra (EE).

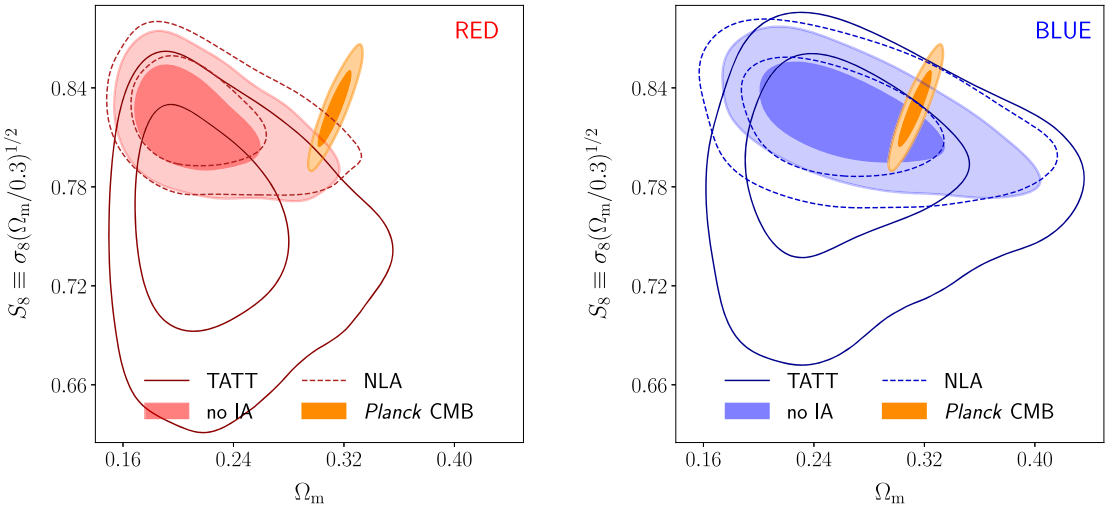


FIG. 4. Marginalized posteriors for $\Omega_m$ and $S_8$ using the impure RED (left) and pure BLUE (right) samples. For each sample, we consider an analysis with no intrinsic alignment model (filled), with the single parameter NLA model (dashed, unfilled) and the TATT model (solid, unfilled). For reference, we show the *Planck* TTTEEE likelihood [orange, [55] ]. The inner and outer contours correspond to 68% and 95% confidence levels, respectively.

TABLE II. Cosmological results for the FULL, RED, and BLUE samples as mean and *maximum a posteriori* (MAP) values, with the goodness of fit, $\chi^2_{red} = \chi^2_{min}/(N_{data} - N_{par})$. $N_{data} = 400$ for the full scale extent of the measurements and 273 with scale cuts (noted as [a]), and we estimate the effective number of free parameters as $N_{par} \sim [5, 3, 2.5, 2]$ for [TATT, NLA-$z$, NLA and no IA], respectively, as per Refs. [5,56]. The $\chi^2_{min}$ are substantially improved for the BLUE sample (lower than that for FULL, RED by ∼20, 40) and the BLUE cosmological constraints are more stable across IA model choices. The Bayesian evidence ratio with respect to NLA shows that no IA model is preferred for all samples. The differences compared to *Planck* [55] (Table 17, $S_8 = 0.828(16)$, $\Omega_m = 0.3135(81)$ updated from Ref. [6]), $\delta S_8, \delta\Omega_m$, are smallest for the BLUE sample.

| Model | $S_{8,mean}$ | $\Omega_{m,mean}$ | $S_{8,MAP}$ | $\Omega_{m,MAP}$ | Evid. Ratio | $\chi^2_{min}$ | $\chi^2_{red}$ | $\delta S_8$ | $\delta\Omega_m$ | $\sqrt{\delta S_8^2 + \delta\Omega_m^2}$ |
|---|---|---|---|---|---|---|---|---|---|---|
| FULL NLA ($a_1$) | $0.811^{+0.016}_{-0.019}$ | $0.255^{+0.031}_{-0.051}$ | 0.825 | 0.230 | 1.0 | 403.3 | 1.0 | 0.72 | 1.29 | 1.48 |
| FULL NLA-$z$ ($a_1$, $\eta_1$) | $0.804^{+0.023}_{-0.018}$ | $0.249^{+0.029}_{-0.048}$ | 0.823 | 0.208 | 1.5 | 404.0 | 1.0 | 0.87 | 1.51 | 1.74 |
| **(2) FULL TATT** | $0.788^{+0.033}_{-0.025}$ | $0.247^{+0.030}_{-0.044}$ | 0.778 | 0.240 | 0.8 | 399.5 | 1.0 | 1.16 | 1.72 | 2.08 |
| FULL No IA | $0.811^{+0.017}_{-0.019}$ | $0.255^{+0.028}_{-0.042}$ | 0.826 | 0.228 | 20.4 | 403.9 | 1.0 | 0.72 | 1.53 | 1.69 |
| FULL NLA-$z$, Y3 Scale Cuts[a] | $0.793^{+0.027}_{-0.019}$ | $0.267^{+0.035}_{-0.059}$ | 0.801 | 0.250 | | 299.8 | 1.1 | 1.21 | 0.92 | 1.52 |
| **(3) FULL TATT, Y3 Scale Cuts**[a] | $0.777^{+0.035}_{-0.024}$ | $0.273^{+0.035}_{-0.052}$ | 0.776 | 0.308 | | 293.1 | 1.1 | 1.42 | 0.90 | 1.68 |
| RED NLA ($a_1$) | $0.822^{+0.022}_{-0.022}$ | $0.218^{+0.017}_{-0.045}$ | 0.868 | 0.161 | 1.0 | 426.4 | 1.1 | 0.24 | 2.40 | 2.41 |
| RED NLA-$z$ ($a_1$, $\eta_1$) | $0.820^{+0.021}_{-0.023}$ | $0.221^{+0.020}_{-0.048}$ | 0.857 | 0.162 | 0.7 | 424.5 | 1.1 | 0.28 | 2.24 | 2.25 |
| RED TATT | $0.753^{+0.050}_{-0.035}$ | $0.224^{+0.022}_{-0.049}$ | 0.789 | 0.201 | 3.7 | 419.2 | 1.1 | 1.57 | 2.16 | 2.67 |
| RED No IA | $0.818^{+0.019}_{-0.020}$ | $0.215^{+0.017}_{-0.041}$ | 0.862 | 0.167 | 5.9 | 425.1 | 1.1 | 0.39 | 2.76 | 2.79 |
| RED NLA-$z$, Y3 Scale Cuts[a] | $0.792^{+0.029}_{-0.028}$ | $0.238^{+0.021}_{-0.061}$ | 0.826 | 0.182 | | 302.8 | 1.1 | 1.07 | 1.43 | 1.79 |
| RED TATT, Y3 Scale Cuts[a] | $0.762^{+0.049}_{-0.029}$ | $0.231^{+0.023}_{-0.055}$ | 0.752 | 0.175 | | 301.5 | 1.1 | 1.41 | 1.73 | 2.23 |
| BLUE NLA ($a_1$) | $0.820^{+0.023}_{-0.024}$ | $0.262^{+0.035}_{-0.062}$ | 0.819 | 0.254 | 1.0 | 380.2 | 1.0 | 0.28 | 0.95 | 0.99 |
| BLUE NLA-$z$ ($a_1$, $\eta_1$) | $0.811^{+0.032}_{-0.024}$ | $0.260^{+0.038}_{-0.071}$ | 0.821 | 0.238 | 1.6 | 380.6 | 1.0 | 0.49 | 0.91 | 1.04 |
| BLUE TATT | $0.793^{+0.044}_{-0.030}$ | $0.266^{+0.034}_{-0.064}$ | 0.813 | 0.269 | 0.6 | 375.4 | 1.0 | 0.79 | 0.87 | 1.18 |
| **(1) BLUE No IA** | $0.822^{+0.019}_{-0.020}$ | $0.268^{+0.031}_{-0.056}$ | 0.810 | 0.260 | 12.7 | 380.9 | 1.0 | 0.23 | 0.95 | 0.98 |
| BLUE NLA-$z$, Y3 Scale Cuts[a] | $0.770^{+0.059}_{-0.025}$ | $0.274^{+0.045}_{-0.070}$ | 0.696 | 0.181 | | 259.0 | 1.0 | 1.10 | 0.64 | 1.27 |
| BLUE TATT, Y3 Scale Cuts[a] | $0.754^{+0.070}_{-0.034}$ | $0.292^{+0.044}_{-0.072}$ | 0.771 | 0.351 | | 252.9 | 0.9 | 1.22 | 0.35 | 1.26 |

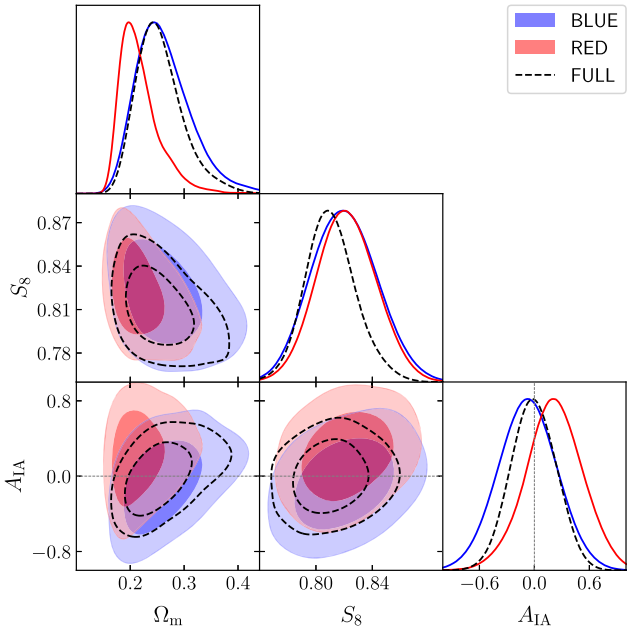


FIG. 5. Intrinsic alignment amplitudes for the single parameter NLA model in the RED (shaded), BLUE (shaded), and FULL (black, dashed) samples, with $1\sigma$ and $2\sigma$ contours plotted for each. We find the all samples to be consistent with no IA; $a_1 = 0$.

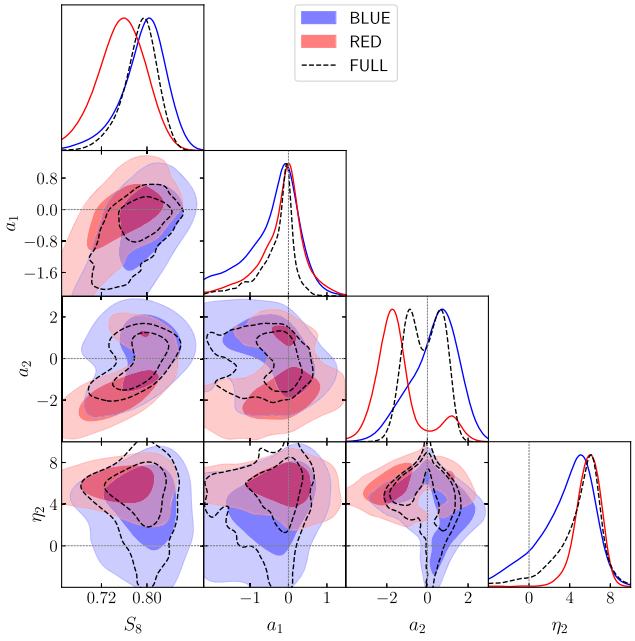


FIG. 6. Constraints on the intrinsic alignment amplitudes, $a_{1,2}$ and redshift evolution, $\eta_2$, TATT model parameters using the RED, BLUE, and FULL (black) samples, with ($1\sigma$ and $2\sigma$ contours). We find the BLUE sample is consistent with zero in both $a_1$, $a_2$, while the RED sample prefers a negative, strongly redshift-evolving $a_2$ amplitude with negligible $a_1$.

the three IA model cases can vary by up to $1.4\sigma$. The BLUE shear analysis is also best described by the ΛCDM model, with the goodness-of-fit for each sample and model quantified in Table II. We approximately report $\chi^2_{\rm red}$ based upon the estimation of effective degrees of freedom in Ref. [1,5], from the minimum $\chi_2$ in the chain. The BLUE sample has $p \geq 0.70$ across all model choices, while FULL ($p \leq 0.43$) and RED ($p \leq 0.20$) are low in comparison, indicating their data are less well described by any model choice.

We compare our constraints on $S_8$ and $\Omega_{\rm m}$ to the *Planck* CMB [55] parameters and report shifts as $\delta S_8$ and $\delta\Omega_{\rm m}$.[7] We find that BLUE is in moderately improved statistical agreement with *Planck* compared to RED and FULL, in all IA model cases. In particular, BLUE: no-IA has $\delta S_8 = 0.23$, while the full has $\delta S_8 = 0.72$ and the impure RED sample has $\delta S_8 = 0.39$. These improvements are mild until we consider $\Omega_{\rm m}$. Cosmic shear analyses that include the small-scale measurements have reported low values of the matter density parameter compared to *Planck* [e.g., [11,57]], which is stable to baryon feedback models [11]. The BLUE $\Omega_{\rm m}$ constraint is consistent with *Planck* within $1\sigma$. For FULL and RED, where we expect galaxies to intrinsically align, we find $\delta\Omega_{\rm m} > 1.5\sigma, 2.1\sigma$, with no improvement when considering more complex IA models (see Table II). Given that IA produces a scale dependent effect, and that the IA models have not been sufficiently validated on the scales that cosmic shear is most sensitive to, it is plausible that IA mismodeling would result in a biased value of $\Omega_{\rm m}$, in addition to $S_8$.

For all samples, Bayesian evidence ratios prefer no intrinsic alignment. The strength of that model preference depends on sample, and is weakest for the RED sample. In the FULL and pure BLUE sample, it is strongly preferred (with the latter yielding Bayes evidence ratio $K = 7.9 \pm 1.2$ over the second highest preference in NLA-$z$). This strong model preference in the FULL sample was also seen in the fiducial analysis [1,5].

### A. Intrinsic alignment parameters

The constraints on the alignment amplitude for NLA are shown in Fig. 5. The RED sample fits for a slightly positive $a_1$, though is consistent with zero at the level of 1-$\sigma$, and the blue and full samples both infer no intrinsic alignment. The TATT model parameters are shown in Fig. 6 for all three samples. Again, the blue sample is consistent with zero IA; $a_1$, $a_2 = 0$ (dashed lines), where $a_2$ is the physically anticipated quadratic alignment mechanism for spirals. In this more complex model, the RED sample also finds zero alignment amplitude but prefers a negative tidal torquing amplitude $a_2$, with a very strong redshift evolution that

[7]For simplicity, we quantify the shifts in the measured values of $S_8$ and $\Omega_{\rm m}$ between two analyses using $\delta X = \Delta X/[(\sigma^1_X)^2 + (\sigma^2_X)^2]^{1/2}$, where $\Delta X$ is the difference between the respective mean values and $\sigma^1_X$,$\sigma^2_X$ are the standard deviations of the two constraints.

becomes extreme at high redshift ($z > 1.5$) and does not map well on to the constituent galaxy populations within each bin. The extreme evolution term appears to be preferred as it allows the model to fit the small-scale behavior in the highest redshift bin autocorrelation while fitting approximately no tidal torquing on all other lower redshift measurements. This $a_1 = 0$ deviates from the literature (e.g., [40]), although we note that the impure RED selection we make differs from past work. We find a degeneracy (1) in response to sign flips in $a_1/a_2$ (as seen in Ref. [1,5]), as well as (2) between high alignment, low-$S_8$ and low alignment, high-$S_8$ models for the impure RED sample specifically. No intrinsic alignment is only slightly preferred for this sample according to the Bayesian evidence ratios ($K = 1.3 \pm 1.2$ w.r.t. TATT), while it is substantially preferred in the other samples (see Table II).

## IV. CONCLUSIONS

The modeling of intrinsic alignments in weak lensing studies is challenging: the model choice between NLA and TATT tends to shift the cosmological constraints by $>0.5\sigma$ [e.g., [5,8,11,58] ]. Application of these models to cosmic shear is challenging as they have thus far only been tested against direct measurements on larger scales and lower redshifts than cosmic shear measurements are sensitive to (6 Mpc$/h$ and $k \sim 1$ for NLA and 2 Mpc$/h$ and $k \sim 3$ for TATT). As progress is made to build flexible baryon feedback models that allow for the analysis of the full scale dependence of shear measurements, the uncertainty in small scale IA modeling is more apparent. Furthermore, the more accurate TATT model incurs additional model parameters that weaken cosmological precision. Newer models [23–25,28,29] could exacerbate that cost.

Red and blue galaxy populations exhibit clear differences in their IA properties. Motivated by the fact that IA have not yet been detected for blue galaxies [e.g., [36] ], which dominate a weak lensing sample, we explore a novel approach for IA mitigation: we select a BLUE IA clean sample, which we assume is negligibly impacted by IA based on current direct IA measurements. First, we assess the stability of cosmological constraints with different IA model choices when using the BLUE sample. Next, we compare the cosmological constraints and goodness of fit of three major analyses: (1) the proposed approach to use all angular scales and a flexible feedback model, but limiting to the BLUE galaxies to mitigate IA, (2) using all angular scales of the DES Y3 FULL sample measurement and a flexible feedback model, with the TATT model for IA, and (3) the fiducial DES Y3 approach to cut the small-scale shear measurements of the FULL sample and model IA with the TATT model—see Fig. 3 for the cosmological results, alongside a popular alternative approach with scale-cuts and the NLA model.

In summary, we extract and analyze a high purity ($\gtrsim$97%) star-forming selection (BLUE) and the complementary color selected sample containing a large fraction ($\sim$30%) of passive, quiescent galaxies (RED). To do this, we repeat the DES Y3 data calibration and cosmic shear analysis. We find that

(i) Restricting the analysis to the BLUE sample of star-forming galaxies produces cosmological constraints that are more stable to IA model choice (even with use of all angular scales), varying by $\sim 0.5\sigma$ in $S_8$. In contrast, the impure RED sample has a best fit cosmology that changes with choice of IA model by $\sim 1.5\sigma$ in $S_8$.

(ii) The $\chi^2_{\rm min}$ are substantially improved for the BLUE sample (lower than that for FULL, RED by $\sim$20, 40). Specifically, the proposed BLUE analysis of (1), that uses all angular scales of the measurement and does not have free IA parameters gives a better fit to the data compared to the FULL sample analyzed with TATT, either with small scales (2) or without (3). The RED sample has the highest $\chi^2_{\rm min}$ for every analysis variant.

(iii) The constraints from the BLUE analysis are in better agreement with results from *Planck* CMB in both $S_8$ and $\Omega_{\rm m}$ compared to the FULL sample analyses (2) and (3). We find $S_8 = 0.822^{+0.019}_{-0.020}$ and $\Omega_{\rm m} = 0.268^{+0.031}_{-0.056}$ as our 68% confidence regions, corresponding to 0.23 in $\delta S_8$. The corresponding full analyses have $\delta S_8 \gtrsim 1.1$ (see Table II).

(iv) Our proposed BLUE IA-mitigation strategy improves the cosmological precision compared to the DES Y3 analysis using the FULL sample and TATT model by a factor of 1.5. That is, the approach of (1) to safely analyze the full angular scale extent with a flexible feedback model and a BLUE sample, where the latter circumvents the concern of IA model suitability, results in a reduced $S_8$ 68% quantile compared to the full sample with TATT, using a feedback model (2) or scale cuts (3).

(v) The BLUE sample IA parameter constraints are consistent with zero amplitude in both NLA and TATT, and the analysis that neglects to model IA is strongly preferred. Consistent with [5], we find this preference for all three samples, although it is very mild for the impure RED sample over TATT (evidence ratio $\approx$1.3). When we do model alignment in the RED sample, TATT finds strong tidal torquing (a negative $a_2$) with an unexpected, extreme redshift evolution (high $\eta_2$).

(vi) All alignment models for the RED sample prefer a low $\Omega_{\rm m}$ and higher $\chi^2$ than the uncontaminated BLUE sample, indicating that no model well describes the alignment in this color-redshift space, and that use of the full sample at affected scales—which contains these poorly modeled contaminants—is ill-advised.

The next generation of weak lensing experiments has arrived. The Vera Rubin [59], Euclid [60], and Roman [61]

Observatories will provide unprecedented quantities of data at unprecedented depth. Current weak lensing efforts have unveiled a deep need to understand and model systematics, among them IA as one of the chief confounding factors. A BLUE cosmic shear analysis, as described here, is a reliable way to account for our limited knowledge on IA. There are promising avenues to progress intrinsic alignment modeling—for example, via direct measurements with spectroscopic surveys and shape measurement (e.g., [21,36,62]) or more flexible models that reduce constraining power (e.g., [30]). However, given our present limited understanding and the ambiguity in model choice, we suggest that selection on blue galaxies allows us to perform precision weak lensing analyses with our surveys as they exist today while the ambiguity of model choice clarifies with observation. While we note that complete nonalignment in blue galaxies is not yet measured for all the scales, masses, and redshifts probed by weak lensing surveys, this blue shear analysis serves as the simplest implementation of informative, observation-driven priors on alignment, taking into account galaxy properties like color and redshift and laying the groundwork for more complex exploration of the galaxy sample selection and tailored priors on alignment in the future.

## ACKNOWLEDGMENTS

J. McCullough, A. Amon, E. Legnani, and D. Gruen completed the analysis and wrote the manuscript for this paper with the constructive feedback of A. Roodman. The other core authors, including O. Friedrich, N. MacCrann, and M. Becker, and J. Myles, contributed code and expertise to compute the covariance, to generate the DES Y3 image simulations and compute the shear calibration, and to calibrate the photometric redshifts, respectively. The document has been through internal review within the DES collaboration with S. Dodelson and S. Samuroff acting as internal reviewers with valuable expertise, as well as notable feedback throughout the process from J. Blazek and J. Prat. The remaining authors have made contributions to the Y3 Key Project analysis pipeline, including but not limited to DES instruments, data collection, processing and calibration, and various analysis pipelines. Funding for the DES Projects has been provided by the DOE and NSF(USA), MEC/MICINN/MINECO (Spain), STFC (UK), HEFCE (UK). NCSA (UIUC), KICP (U. Chicago), CCAPP (Ohio State), MIFPA (Texas A&M), CNPQ, FAPERJ, FINEP (Brazil), DFG (Germany) and the Collaborating Institutions in the Dark Energy Survey. The Collaborating Institutions are Argonne Lab, UC Santa Cruz, University of Cambridge, CIEMAT-Madrid, University of Chicago, University College London, DES-Brazil Consortium, University of Edinburgh, ETH Zürich, Fermilab, University of Illinois, ICE (IEEC-CSIC), IFAE Barcelona, Lawrence Berkeley Lab, LMU München and the associated Excellence Cluster Universe, University of Michigan, NFS NOIRLab, University of Nottingham, Ohio State University, University of Pennsylvania, University of Portsmouth, SLAC National Lab, Stanford University, University of Sussex, Texas A&M University, and the OzDES Membership Consortium. Based in part on observations at NSF Cerro Tololo Inter-American Observatory at NSF NOIRLab (NOIRLab Prop. ID 2012B-0001; PI: J. Frieman), which is managed by the Association of Universities for Research in Astronomy (AURA) under a cooperative agreement with the National Science Foundation. The DES Data Management System is supported by the NSF under Grants No. AST-1138766 and No. AST-1536171. The DES participants from Spanish institutions are partially supported by MICINN under Grants No. PID2021-123012, No. PID2021-128989, No. PID2022-141079, No. SEV-2016-0588, No. CEX2020-001058-M, and No. CEX2020-001007-S, some of which include ERDF funds from the European Union. IFAE is partially funded by the CERCA program of the Generalitat de Catalunya. We acknowledge support from the Brazilian Instituto Nacional de Ciência e Tecnologia (INCT) do e-Universo (CNPq Grant No. 465376/2014-2). This manuscript has been authored by Fermi Research Alliance, LLC under Contract No. DE-AC02-07CH11359 with the U.S. Department of Energy, Office of Science, Office of High Energy Physics. This work has benefitted from support by the Deutsche Forschungsgemeinschaft (DFG, German Research Foundation) under Germany's Excellence Strategy—EXC-2094–390783311 and by the Bavaria California Technology Center (BaCaTec).

## DATA AVAILABILITY

The data that support the findings of this article are openly available [79].

## APPENDIX A: SELECTION AND PURITY OF BLUE SAMPLE

As seen in Fig. 7, we can use template fits run in the deep field from e.g., BAGPIPES and the BALROG transfer function (see Ref. [47]) to describe how realizations of red galaxies populate the lower-dimensional, $riz$ color space where we must perform our selection. The process of performing this inference on fractional purity, or the probability of being red $p(r)$, for a wide SOM color cell $\hat{c}$, that comprises part of a tomographic bin, $\hat{c} \in b$, follows as a function of deep field SOM color cells $c$, and our overall selection in those deep fields, $\hat{s}$, as

$$p(r|b,\hat{s}) = \sum_{\hat{c}\in b}\sum_{c} p(r|c,\hat{s})p(c|\hat{c},\hat{s})p(\hat{c}|\hat{s}), \qquad \text{(A1)}$$

where we define

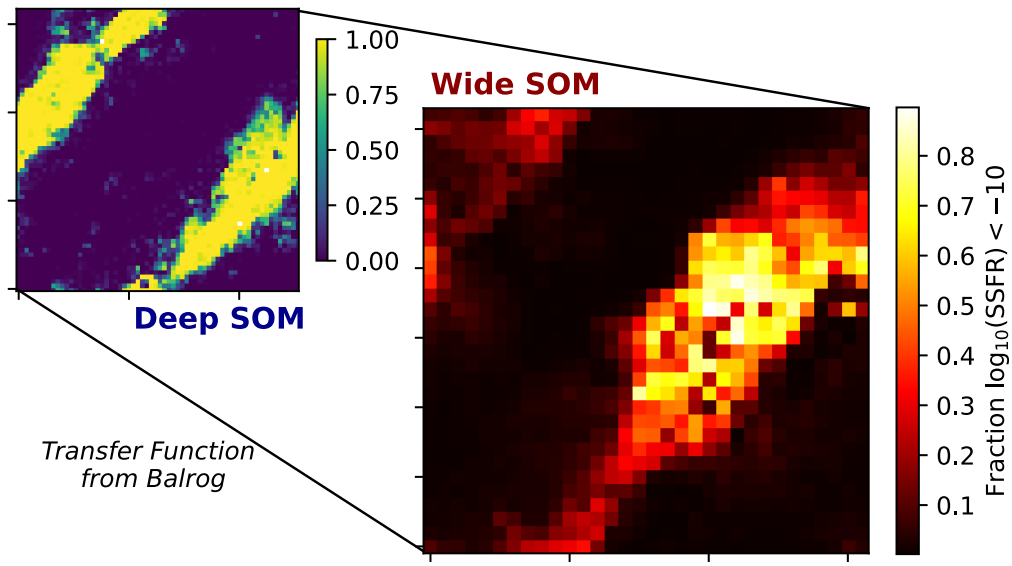


FIG. 7. Depiction of the passive galaxy contamination of our selection, propagated from a cut on SSFR in the deep fields through the SOMPZ transfer function generated with an injected BALROG sample. The contamination in our bin selections are described in Table I.

(i) $p(\hat{c}|\hat{s})$ as the overall abundances of galaxies in a given wide cell given our selection and can be written in terms of cell occupancies,
(ii) $p(c|\hat{c},\hat{s})$ as our transfer function from BALROG,
(iii) $p(r|c,\hat{s})$ as the determination from deep field photometry on how likely a galaxy in a given deep color cell is to be passive, nonstar-forming, or *red*.

The latter term can be estimated several ways given high resolution deep field data, and we presented three such potential metrics in Table I. Our criteria for red contamination in each case is defined below:

(i) BAGPIPES: Bayesian Analysis of Galaxies for Physical Inference and Parameter Estimation (BAGPIPES[8]) is a Bayesian SED fitting code that models the emission from galaxies in a broad range of wavelengths, fits these models to observational data, and generates multivariate posterior distributions of various galaxy physical properties (e.g., SSFR, stellar mass). Its ability to recover realistic properties has been studied comprehensively in simulations [49]. We define our passive contamination by simply taking the galaxies where the best fit specific star formation rate, `ssfr_best`, is very low, i.e.,

$$\log_{10}(\mathrm{SSFR}) < -10. \tag{A2}$$

See the deep to wide mapping of this selection in Fig. 7.

(ii) EAZY: As a SED fitting code for photo-$z$ estimation, EAZY [50] supplies coefficients for a suite of semi-analytically modeled basis templates. We define our red contamination as galaxies where the sum of best fit coefficients $A_t$ for the passive templates $t \in P$, is dominant over all templates $t$. Our exact threshold was chosen to naturally bisect the visible bimodal distribution

$$\sum_{t\in P} A_t \geq 0.77 \sum_{t} A_t. \tag{A3}$$

(iii) Balmer: As this inference framework is being done where we have high confidence spectroscopic and narrow band redshifts (i.e., a well defined color-redshift relation), we can identify passive galaxies by their anticipated large balmer break color. With the deep SOM median redshift, we identify where the Balmer break at $(1+z)\times 4000$. We then take the filters (in deep, from *ugrizJHK*) on either side of the Balmer break (e.g., $u-r$, $i-Y$) as our color $BB_c$, where passive galaxies are liable to have a steep slope and select on

$$BB_c > 2.0. \tag{A4}$$

This particular method identifies a larger fraction of "red" contaminants, but agrees with the prior two methods on which cells are most contaminated.

## APPENDIX B: DATA CALIBRATION

To perform a measurement on cosmic shear, we must (1) understand the redshift distribution of the source galaxies and (2) understand the statistical relationship between a galaxy's shape and the true shear. To tackle (1), in Sec. B 1, we implement a hierarchical Bayesian inference scheme that informs photometric redshifts with

[8]https://bagpipes.readthedocs.io.

TABLE III. The calculated m priors in each bin from the image simulations (*sim* or reported in Ref. [1] as *noz-blend*) and resulting final shear bias $m$, when the simulation calibration is applied to DES data.

| | FULL | RED | BLUE |
|---|---|---|---|
| $m_{1,\mathrm{sim}} \times 100$ | $-1.362 \pm 0.296$ | $-1.006 \pm 0.473$ | $-1.156 \pm 0.419$ |
| $m_{2,\mathrm{sim}} \times 100$ | $-1.764 \pm 0.359$ | $-2.106 \pm 0.460$ | $-1.158 \pm 0.623$ |
| $m_{3,\mathrm{sim}} \times 100$ | $-2.488 \pm 0.417$ | $-2.369 \pm 0.512$ | $-2.277 \pm 0.777$ |
| $m_{4,\mathrm{sim}} \times 100$ | $-3.350 \pm 0.513$ | $-3.371 \pm 0.989$ | $-3.292 \pm 0.722$ |
| $m_{1,\mathrm{final}} \times 100$ | $-0.783 \pm 0.361$ | $-0.890 \pm 0.339$ | $-1.288 \pm 0.329$ |
| $m_{2,\mathrm{final}} \times 100$ | $-1.737 \pm 0.329$ | $-1.782 \pm 0.309$ | $-1.799 \pm 0.388$ |
| $m_{3,\mathrm{final}} \times 100$ | $-2.343 \pm 0.262$ | $-2.366 \pm 0.277$ | $-2.031 \pm 0.680$ |
| $m_{4,\mathrm{final}} \times 100$ | $-3.479 \pm 0.285$ | $-3.147 \pm 0.577$ | $-3.560 \pm 0.363$ |

well-known spectroscopic redshifts in limited fields. In order to characterize (2), in Sec. B 2, we rely on a set of image simulations that can inject true galaxy shapes from a high-resolution imaging survey and apply shears to those shapes, before remeasuring them as the original instrument would. Due to blending, this results in small shifts of our redshift distributions described in Sec. B 3. Lastly, we estimate covariance in Sec. B 4.

### 1. Redshift calibration

We follow the SOMPZ procedure outlined in Ref. [63], as implemented in Ref. [45] with a each tomographic bin split into a RED and BLUE sample by their $r-z$ color (SOM cell assignment, see Fig. 1 inset panels). The redshift distributions for each original tomographic bin, as well as the splits on color are seen in Fig. 1, following the same procedure for redshift inference from the same sources as Ref. [45] (see the fiducial *SPC, PC, SC* sample).

As demonstrated in Ref. [1], combining redshift inference from SOMPZ with clustering redshifts provided no substantial shifts in cosmology. Therefore we simplify our analysis with a single realization of the tomographic $N(z)$ s from SOMPZ (i.e., no use of many realizations in HYPERRANK), and no addition of clustering redshifts (WZ) or shear ratios (SR). As the pipeline was extensively validated in DES Y3, we match the uncertainty on mean redshift per bin developed in [45], and shift the mean redshifts according to our new sample selection.

### 2. Shear calibration

We repeat in part the analysis in Ref. [48] for DES Y3 on the same suite of image simulations to provide corrections in the form of a multiplicative bias on the METACALIBRATION response. The simulations include catalogs with an applied constant shear ($\pm g_{1,2}$) and an applied shear in each of four bins of true redshift, or $z$-slice, with bounds [0.0, 0.4, 0.7, 1.0, 3.0]. The latter allows for an estimation of the effect of redshift-dependent shear bias, which is largely believed to be the result of contributions from blending. This enters our analysis as a modification of the redshift distribution $n_\gamma(z)$, which will contribute per bin a mean multiplicative factor, $m$, and a shift in mean redshift, $\Delta\bar{z}$.

We make use of a simplification of the alternative tomographic binning technique (see Ref. [48] Sec. 3.7) to marginalize over for the final reported multiplicative bias. The two choices of binning are:

(i) *Fiducial (fid)*: applies the same SOM cell-bin mapping as in the data analysis.

(ii) *Abundance-weighting (weight)*: applies the same mapping as with the fiducial, but accounts for variation in the colors and distributions of galaxy populations between the simulations and data. This binning reweights contributions on a cell-by-cell basis according to $N_{\mathrm{data},c}/N_{\mathrm{sim},c}$ (so-dubbed *w-match* in Ref. [48]).

As we will apply an overly conservative shear bias in this analysis, additional tomographic binning systems will not be applied, nor will the near-neighbor reweighting (done to approximate clustering in the simulation suite as was computed for the DES Y3 gold sample analysis). This simplified approach is feasible only because shear calibration is not the driving systematic in the DES Y3 cosmology analysis. In lieu of these computations, we will simply double our estimation for uncertainty in $m$ and provide a conservative high limit for our shear bias.

### 3. $N_{\mathrm{eff}}(z)$ from shear calibration

Following the shear calibration analysis methodology from DES Y3 in Ref. [48], we produce samples of $f(z)$ and $g(z)$ from measurements in a suite of image simulations that modify our tomographic redshift distributions $N^i(z)$ in bin $i$ to adjust for blending contributions according to a prescription of

$$N^i_\gamma(z) = (1 + f^i(z))N^i(z) + g^i(z), \tag{B1}$$

where $N^i_\gamma$ is the new effective redshift distribution taking into account redshift dependent shear bias. We employed the fiducial (fid.) functional forms of $f$ and $g$ in Ref. [48] (i.e., their Sec. 5.5.1), alongside the alternative f(z) (alt.,

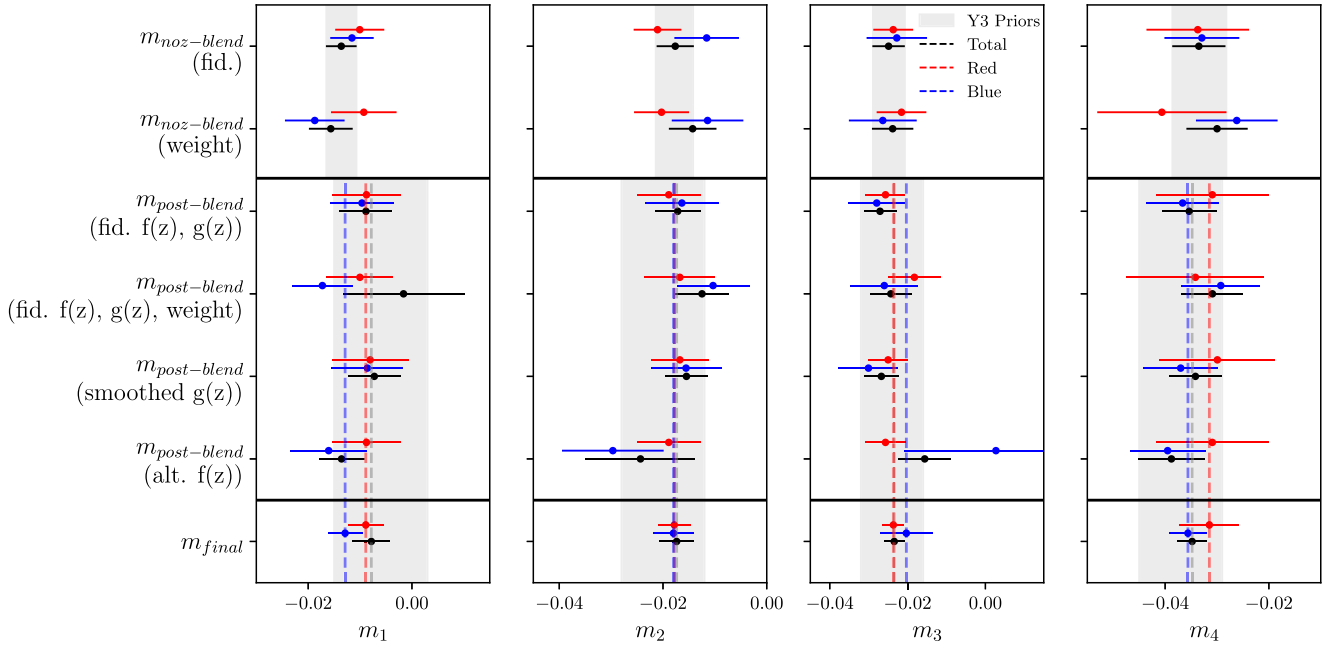


FIG. 8. The recalculated shear bias measurements for RED and BLUE galaxy splits following a simplified form of the analysis in Ref. [48]. Our final shear priors on $m_i$ have the same width as the Y3 priors, but midpoints calculated as $m_{\rm final}$.

Student's-$t$) and the smoothed g(z). We display results on $m_i$ of applying these model fits to the simulations in Fig. 8 and take the combined result for each tomographic bin as our new prior centers for $m_i$. The redshift distributions in Fig. 1 contain these small modifications due to blending. Table III summarizes the final priors on shear bias for the color-selected samples in each tomographic bin as used in the cosmological analyses for this work.

### 4. Covariance

We follow our modeling of the analytic covariance matrix from the analysis in Ref. [64] for DES Y3. The calculations are carried out using CosmoCov [65] for our split samples at the best-fit cosmology from the DES Y3 $3\times2$pt analysis that combined cosmic shear, galaxy-galaxy lensing, and clustering in Ref. [54]. This covariance matrix was computed with tomographic effective number densities and average per-component shape noise quoted in Table I and calibrated redshift distributions for all samples: FULL, BLUE, RED.

## APPENDIX C: SAMPLING COSMOLOGY

### 1. Cosmic shear

We can model our two-point correlation functions in shear by first beginning with the three dimensional nonlinear matter power spectrum. This is written in terms of the two-dimensional convergence power spectrum from lensing, $C_\kappa^{i,j}$, which can be defined at a given angular wave number $\ell$ as a decomposition into E-modes and B-modes,

$$\xi_\pm(\theta)=\sum_\ell \frac{2\ell+1}{4\pi}G_\ell^\pm(\cos\theta)(C^{ij}_{\kappa,\rm EE}(\ell)\pm C^{ij}_{\kappa,\rm BB}(\ell)). \tag{C1}$$

While weak lensing will not contribute to $C_{\kappa,\rm BB}$, intrinsic alignment can. Spherical harmonics in Ref. [66] provide

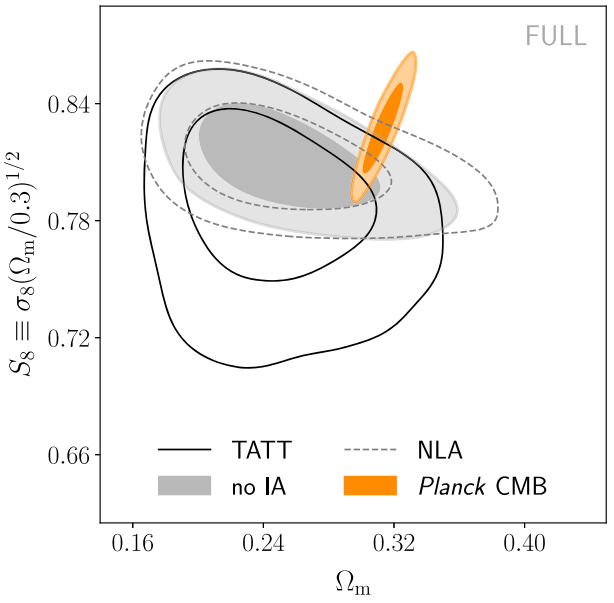


FIG. 9. Marginalized posteriors for $\Omega_{\rm m}$ and $S_8$ using the FULL sample, using all measured scales with the same models found in Fig. 4.

TABLE IV. Summary of cosmological, observational and astrophysical parameters and priors used in the analysis. In the case of flat priors, indicated by square bracketsm the prior bound to the range indicated in the value column. Gaussian priors are indicated by brackets, and are described as (mean, 1-$\sigma$ width).

| Parameter | Value | |
|---|---|---|
| *Cosmological* | | |
| $\Omega_m$, Total matter density | [0.1, 0.9] | |
| $\Omega_b$, Baryon density | [0.03, 0.07] | |
| $A_s$, Scalar spectrum amplitude | [0.5, 5.0] $\times 10^{-9}$ | |
| $h$, Hubble parameter | [0.55, 0.91] | |
| $n_s$, Spectral index | [0.87,1.07] | |
| *Baryon Feedback* | | |
| $\log_{10}(T_{AGN})$, Strength of AGN feedback | [7.6, 8.3] | |
| *Intrinsic alignment* | | |
| $a_1$, Tidal alignment amplitude (NLA) | $[-5, 5]$ | |
| $\eta_1$, Tidal alignment $z$-index | $[-5, 5]$ | |
| $a_2$, Tidal torque amplitude | $[-5, 5]$ | |
| $\eta_2$, Tidal torque $z$-index | $[-5, 10]$ | |
| $b_{ta}$, Tidal alignment bias | [0, 2] | |
| *Observational* | *BLUE* | *RED* |
| $\Delta z^1$, Redshift calibration uncertainty 1 | (0.0, 0.018) | (0.0, 0.018) |
| $\Delta z^2$, Redshift calibration uncertainty 2 | (0.0, 0.015) | (0.0, 0.015) |
| $\Delta z^3$, Redshift calibration uncertainty 3 | (0.0, 0.011) | (0.0, 0.011) |
| $\Delta z^4$, Redshift calibration uncertainty 4 | (0.0, 0.017) | (0.0, 0.017) |
| $m^1$, Shear calibration uncertainty 1 | (−0.013, 0.009) | (−0.009, 0.009) |
| $m^2$, Shear calibration uncertainty 2 | (−0.018, 0.008) | (−0.018, 0.008) |
| $m^3$, Shear calibration uncertainty 3 | (−0.020, 0.008) | (−0.024, 0.008) |
| $m^4$, Shear calibration uncertainty 4 | (−0.036, 0.008) | (−0.032, 0.008) |

$G_\ell^\pm$. For ease of computing, we implement the flat-sky and Limber approximations [67], the latter of which is accurate at high multipoles. With this, we can relate our convergence power spectrum from lensing to the overall three-dimensional matter power spectrum $P(k, z)$

$$C_\kappa^{ij}(\ell) = \int_0^{\chi_H} P\left(k = \frac{\ell + 0.5}{\chi(z)}, z\right) \frac{W_i(\chi) W_j(\chi)}{\chi^2} d\chi, \quad \text{(C2)}$$

where $\chi$ is the comoving angular diameter distance, $z$ is the redshift, and $\chi_H$ is the distance to the horizon. The power spectrum is modulated by $W_i(\chi)$, which describes how efficiently it is picked up by lensing in a given tomographic bin. We write these kernels for lensing efficiency as

$$W_i(\chi) = \frac{3H_0^2 \Omega_m \chi}{2c^2 a(\chi)} \int_\chi^{\chi_H} n_i(\chi') \frac{\chi' - \chi}{\chi'} d\chi', \quad \text{(C3)}$$

where $n_i$ is the normalized effective number density of galaxies, $a$ is the scale factor, and both can be written as functions of comoving distance $\chi$.

We therefore have an expression that can relate our observed measurements (shear two-point correlation) to simulated, cosmologically dependent models of the full nonlinear matter power spectrum.

### 2. Modeling IA

The direct quantities that intrinsic alignment models like NLA and TATT must predict are in the space of the two-point function, where our data vector lives. Galaxies can be intrinsically correlated with their neighbors, but also anti-correlated with background galaxies experiencing shear from the massive structure the aligned galaxies share. We can write the angular power spectrum between redshift bins $i$, $j$ in terms of these gravitational, $G$, and intrinsic, $I$, shears

$$\langle \epsilon^{\text{obs},i} \epsilon^{\text{obs},j} \rangle = \langle \gamma_G^i \gamma_G^j \rangle + \langle \gamma_G^i \gamma_I^j \rangle + \langle \gamma_I^i \gamma_G^j \rangle + \langle \gamma_I^i \gamma_I^j \rangle, \quad \text{(C4)}$$

where any terms involving $\epsilon$ at nonzero separation average to zero.

### 3. Calculation and sampling

When running cosmology chains we use the COSMOSIS framework [68–71] and follow the optimal sampler settings derived in Ref. [72], to use POLYCHORD [73,74]. These settings were further confirmed in the joint DES-KiDS analysis [8].

We use CAMB to calculate the linear component of the matter power spectrum [75], and HMCODE2020 for the nonlinear correction [51]. For simplicity, we fix two massless neutrino species and a third with the lowest mass

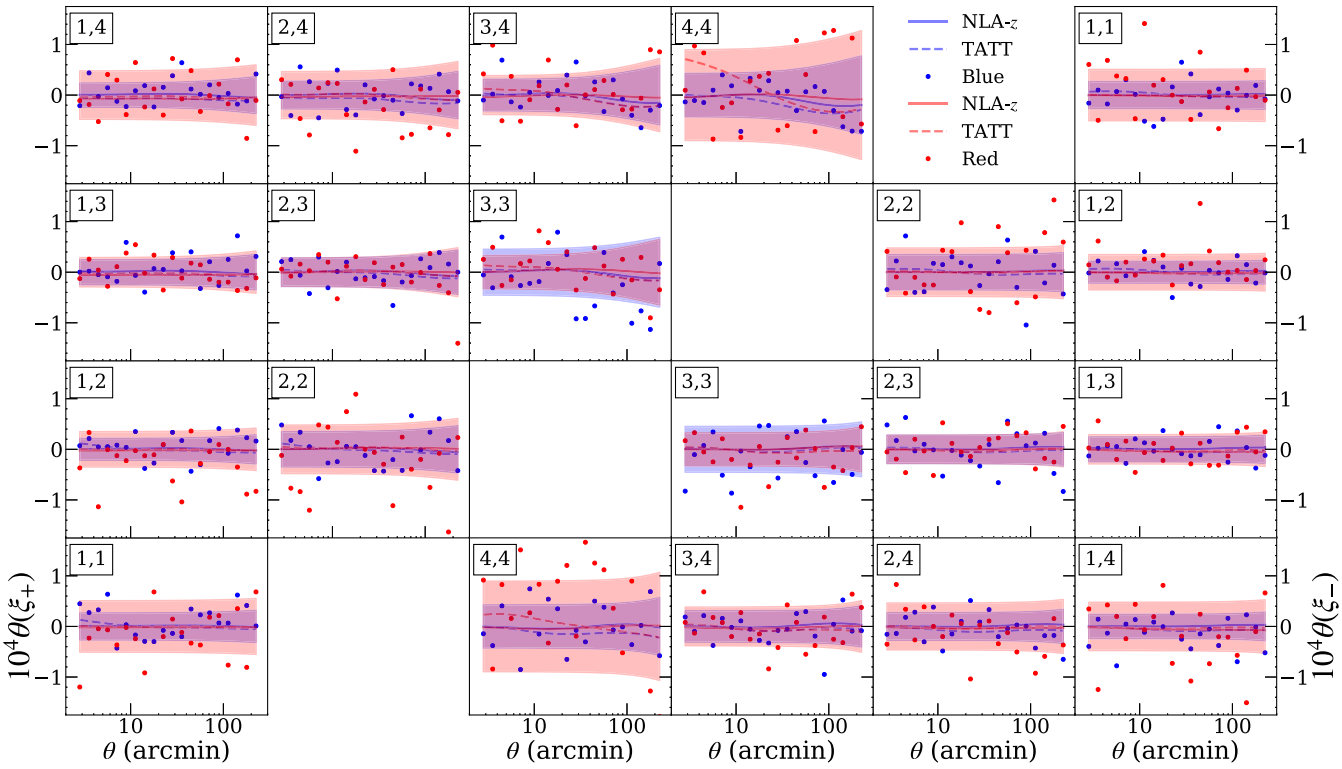


FIG. 10. Cosmic shear two-point correlation residuals between the measurements for the BLUE and RED samples compared to the no IA best fit model. The shaded envelope represents the square root of the diagonal of the analytic covariance matrix. The solid and dashed lines represent residuals computed with the best fit using the NLA and TATT IA models. The differences between the best fits using different IA models are small and within the measurement uncertainty. The most notable shift compared to no IA is with the TATT model in the highest redshift bin.

permitted in oscillation experiments ($m_\nu = 0.06$ eV, e.g., [76]).

We model the baryonic feedback effects according to a wider, higher prior than in previous studies (see Table IV), and with more large-scale impact than accounted for in DES Y3 [7], by taking into account more recent analyses that find the suppression of the nonlinear power spectrum at small scales requires stronger feedback [11,77]. We make use of a parameter within HMCODE2020, $\Theta_{\rm AGN}$, to model this contribution to the correlation function [51]. As a result of this generous prior, and our intention to study competing models of intrinsic alignment, we examine all angular scales of the correlation function.

In Table IV, we record priors on model the uncertainty in mean redshift and the shear calibration for each

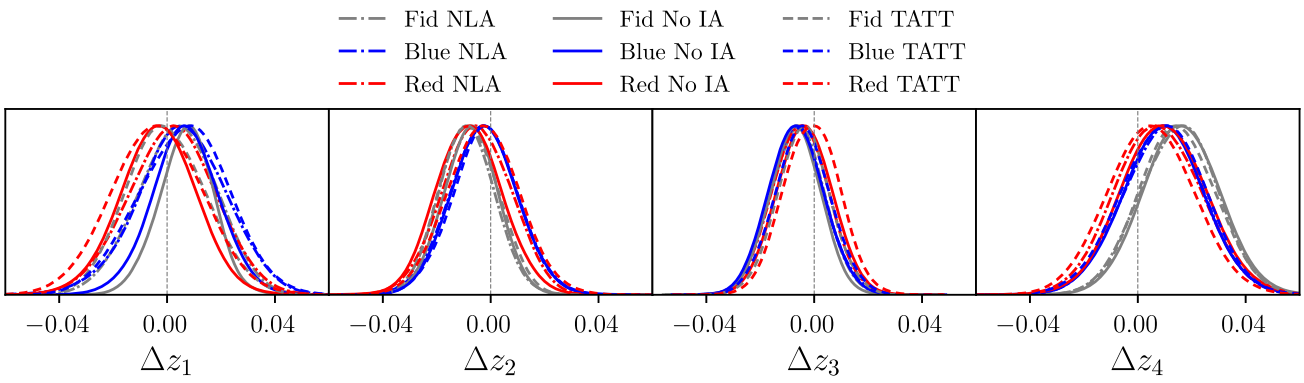


FIG. 11. Posterior distributions for our major samples (FULL, impure RED, pure BLUE) and alignment models (TATT, NLA, No IA) for the mean redshift per tomographic bin. We do not see any major shifts in $\bar{z}_i$ beyond 1-$\sigma$, indicating low degeneracy with IA.

TABLE V. Statistics for the comprehensive suite of Markov Chain Monte Carlo (MCMC) chains run with variations in model choice and sample of galaxies for cosmic shear, a subset of this table is displayed in Table II, where we provide column definitions.

| Model | $S_{8,\mathrm{mean}}$ | $\Omega_{m,mean}$ | Evid. Ratio | $\chi^2_{\mathrm{min}}$ | $\chi^2_{\mathrm{red}}$ | $p$ | $\delta S_8$ | $\delta\Omega_m$ | $\sqrt{\delta S_8^2+\delta\Omega_m^2}$ |
|---|---|---|---|---|---|---|---|---|---|
| FULL NLA-$z$ ($a_1$) | $0.811^{+0.016}_{-0.019}$ | $0.255^{+0.031}_{-0.051}$ | 1.0 | 403.3 | 1.01 | 0.4093 | 0.720 | 1.292 | 1.479 |
| FULL NLA ($a_1$, $\eta_1$) | $0.804^{+0.023}_{-0.018}$ | $0.249^{+0.029}_{-0.048}$ | 1.5 | 404.0 | 1.02 | 0.3934 | 0.866 | 1.511 | 1.742 |
| **(2) FULL TATT** | $0.788^{+0.033}_{-0.025}$ | $0.247^{+0.030}_{-0.044}$ | 0.8 | 399.5 | 1.01 | 0.4271 | 1.159 | 1.722 | 2.076 |
| FULL TATT ($b_{ta}=1.0$) | $0.788^{+0.032}_{-0.027}$ | $0.251^{+0.029}_{-0.045}$ | 0.9 | 399.4 | 1.01 | 0.4282 | 1.169 | 1.572 | 1.959 |
| FULL No IA | $0.811^{+0.017}_{-0.019}$ | $0.255^{+0.028}_{-0.042}$ | 20.4 | 403.9 | 1.01 | 0.4077 | 0.716 | 1.528 | 1.687 |
| FULL NLA, No AGN Feedback | $0.782^{+0.018}_{-0.014}$ | $0.271^{+0.039}_{-0.052}$ | 0.3 | 407.0 | 1.03 | 0.3535 | 1.931 | 0.887 | 2.125 |
| FULL NLA, Y3 Scale Cuts[a] | $0.793^{+0.027}_{-0.019}$ | $0.267^{+0.035}_{-0.059}$ | 1.0 | 299.8 | 1.11 | 0.1029 | 1.208 | 0.917 | 1.517 |
| FULL No IA, Y3 Scale Cuts[a] | $0.794^{+0.018}_{-0.019}$ | $0.269^{+0.034}_{-0.055}$ | 9.0 | 298.9 | 1.10 | 0.1172 | 1.374 | 0.965 | 1.679 |
| **(3) FULL TATT, Y3 Scale Cuts**[a] | $0.777^{+0.035}_{-0.024}$ | $0.273^{+0.035}_{-0.052}$ | 0.9 | 293.1 | 1.09 | 0.1399 | 1.418 | 0.900 | 1.680 |
| RED NLA-$z$ ($a_1$) | $0.822^{+0.022}_{-0.022}$ | $0.218^{+0.017}_{-0.045}$ | 1.0 | 426.4 | 1.07 | 0.1530 | 0.237 | 2.395 | 2.407 |
| RED NLA ($a_1$, $\eta_1$) | $0.820^{+0.021}_{-0.023}$ | $0.221^{+0.020}_{-0.048}$ | 0.7 | 424.5 | 1.07 | 0.1638 | 0.277 | 2.237 | 2.255 |
| RED TATT | $0.753^{+0.050}_{-0.035}$ | $0.224^{+0.022}_{-0.049}$ | 3.7 | 419.2 | 1.06 | 0.1926 | 1.574 | 2.163 | 2.675 |
| RED TATT ($b_{ta}=1.0$) | $0.747^{+0.055}_{-0.036}$ | $0.222^{+0.024}_{-0.051}$ | 2.9 | 418.6 | 1.06 | 0.1987 | 1.587 | 2.075 | 2.612 |
| RED No IA | $0.818^{+0.019}_{-0.020}$ | $0.215^{+0.017}_{-0.041}$ | 5.9 | 425.1 | 1.07 | 0.1673 | 0.393 | 2.759 | 2.787 |
| RED NLA, No AGN Feedback | $0.799^{+0.020}_{-0.017}$ | $0.228^{+0.023}_{-0.051}$ | 0.8 | 426.4 | 1.07 | 0.1487 | 1.169 | 1.977 | 2.297 |
| RED NLA, Y3 Scale Cuts[a] | $0.792^{+0.029}_{-0.028}$ | $0.238^{+0.021}_{-0.061}$ | 1.0 | 302.8 | 1.12 | 0.0830 | 1.071 | 1.433 | 1.789 |
| RED No IA, Y3 Scale Cuts[a] | $0.788^{+0.027}_{-0.025}$ | $0.230^{+0.021}_{-0.055}$ | 5.1 | 302.9 | 1.12 | 0.0891 | 1.344 | 1.788 | 2.236 |
| RED TATT, Y3 Scale Cuts[a] | $0.762^{+0.049}_{-0.029}$ | $0.231^{+0.023}_{-0.055}$ | 0.3 | 301.5 | 1.12 | 0.0781 | 1.414 | 1.728 | 2.232 |
| BLUE NLA-$z$ ($a_1$) | $0.820^{+0.023}_{-0.024}$ | $0.262^{+0.035}_{-0.062}$ | 1.0 | 380.2 | 0.96 | 0.7257 | 0.277 | 0.952 | 0.991 |
| BLUE NLA ($a_1$, $\eta_1$) | $0.811^{+0.032}_{-0.024}$ | $0.260^{+0.038}_{-0.071}$ | 1.6 | 380.6 | 0.96 | 0.7144 | 0.491 | 0.912 | 1.036 |
| BLUE TATT | $0.793^{+0.044}_{-0.030}$ | $0.266^{+0.034}_{-0.064}$ | 0.6 | 375.4 | 0.95 | 0.7540 | 0.788 | 0.872 | 1.175 |
| BLUE TATT ($b_{ta}=1.0$) | $0.790^{+0.051}_{-0.026}$ | $0.267^{+0.036}_{-0.063}$ | 0.5 | 375.9 | 0.95 | 0.7478 | 0.798 | 0.850 | 1.166 |
| **(1) BLUE No IA** | $0.822^{+0.019}_{-0.020}$ | $0.268^{+0.031}_{-0.056}$ | 12.7 | 380.9 | 0.96 | 0.7225 | 0.232 | 0.951 | 0.978 |
| BLUE NLA, No AGN Feedback | $0.791^{+0.032}_{-0.018}$ | $0.277^{+0.041}_{-0.069}$ | 1.1 | 381.6 | 0.96 | 0.7022 | 1.094 | 0.611 | 1.253 |
| BLUE NLA, Y3 Scale Cuts[a] | $0.770^{+0.059}_{-0.025}$ | $0.274^{+0.045}_{-0.070}$ | 1.0 | 259.0 | 0.96 | 0.6743 | 1.102 | 0.637 | 1.273 |
| BLUE No IA, Y3 Scale Cuts[a] | $0.796^{+0.023}_{-0.022}$ | $0.289^{+0.039}_{-0.062}$ | 6.7 | 259.5 | 0.96 | 0.6822 | 1.128 | 0.450 | 1.215 |
| BLUE TATT, Y3 Scale Cuts[a] | $0.754^{+0.070}_{-0.034}$ | $0.292^{+0.044}_{-0.072}$ | 1.1 | 252.9 | 0.94 | 0.7381 | 1.216 | 0.347 | 1.264 |

[a]Chains with optimized Y3 scale cuts (defined in [1,5]) do not model AGN feedback to compare to prior results, $N_{\mathrm{data}}=273$.

tomographic bin $i$ as the free parameters $\Delta z^i$ and $m^i$. We hit prior boundaries in TATT parameter $\eta_2$, and thus extend that prior from $[-5,5]$ to $[-5,10]$, deviating from the fiducial Y3 analysis in Refs. [1,5]. While the physical implication of a redshift evolution term this high is unclear, we expect this is likely a degenerate feature within the TATT model as fitted to our data. We demonstrate residuals of our model fits with respect to the preferred no intrinsic alignment model in Fig. 10.

Our full results are recorded in Table V for all sampled models, and are summarized in Fig. 12 for $S_8$ and $\Omega_{\mathrm{m}}$. The all-scale FULL sample analog for Fig. 4 is depicted in Fig. 9 for comparison, showing overall lower $\Omega_{\mathrm{m}}$ than its scale-cut or BLUE counterparts.

### 4. IA-photo-$z$ interplay

Systematic uncertainty if not properly modeled and understood can be absorbed in other nuisance parameters. IA parameters can be degenerate with uncertain photometric redshift calibration. The effects of this can be visible in posterior distributions for shifts in the mean redshift of each tomographic bin, and intrinsic alignment parameter fits, as have been explored in Ref. [78].

We do not find any major shifts in mean redshift, as depicted in Fig. 11, though the first redshift bin tends to prefer a slightly low $\Delta\bar{z}_1$ in the RED sample and a slightly high $\Delta\bar{z}_1$ in the BLUE, these shifts are cohesive independent of IA model choice. We conclude that any interplay between IA modeling and photo-$z$ calibration is small.

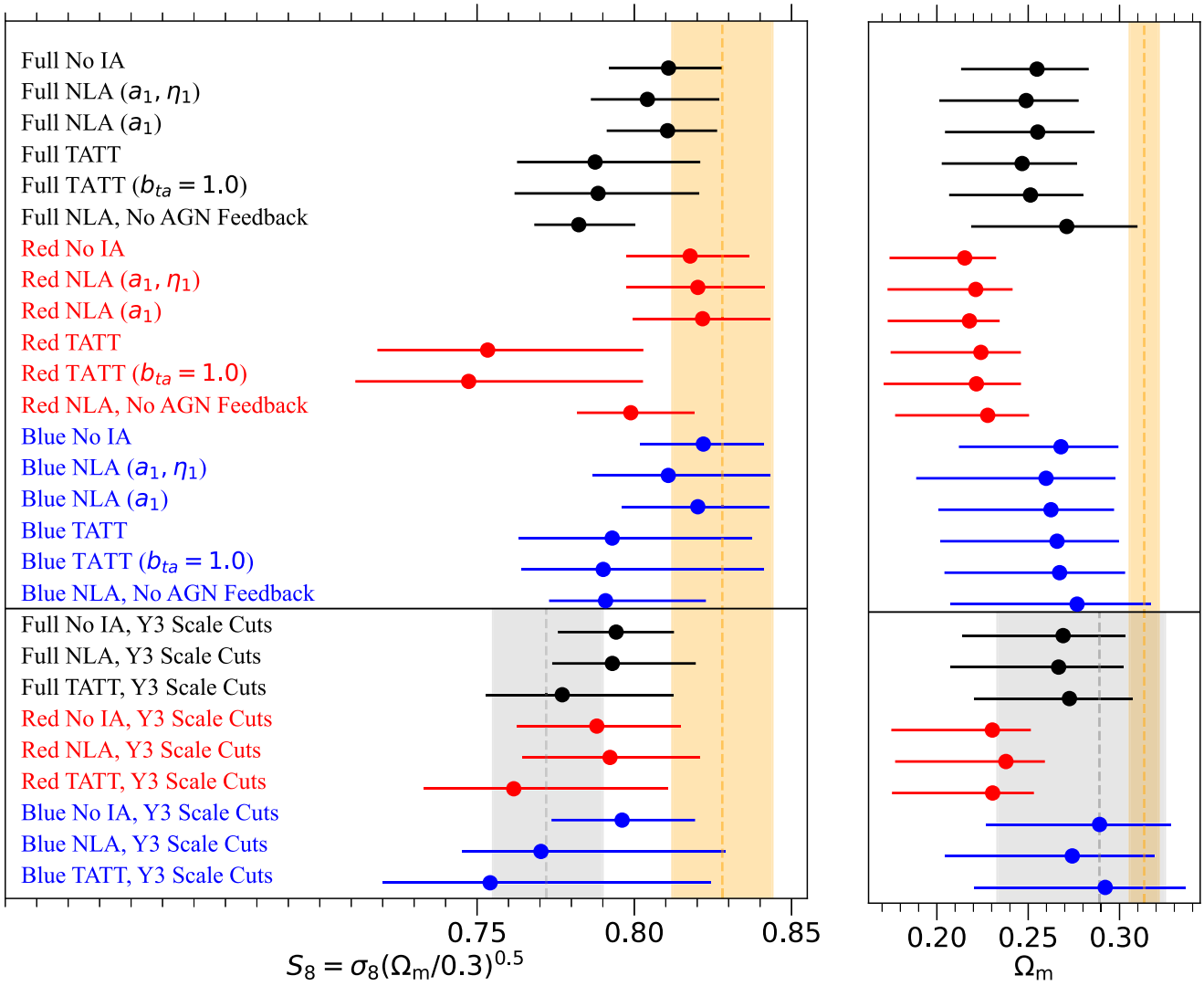


FIG. 12. Summary statistics for each cosmological model fit, with the DES Y3 ΛCDM-optimized result in shaded gray, and the *Planck* results [55] in shaded orange. The 68% confidence regions (1-$\sigma$) are reported for each model fit. Note the DES Y3 fiducial results use a slightly different tomographic binning and prior range.


[1] A. Amon, D. Gruen, M. A. Troxel *et al.*, Dark Energy Survey Year 3 results: Cosmology from cosmic shear and robustness to data calibration, Phys. Rev. D **105**, 023514 (2022).

[2] M. Asgari, C.-A. Lin, B. Joachimi *et al.*, KiDS-1000 cosmology: Cosmic shear constraints and comparison between two point statistics, Astron. Astrophys. **645**, A104 (2021).

[3] R. Dalal, X. Li, A. Nicola *et al.*, Hyper Suprime-Cam Year 3 results: Cosmology from cosmic shear power spectra, Phys. Rev. D **108**, 123519 (2023).

[4] X. Li, T. Zhang, S. Sugiyama *et al.*, Hyper Suprime-Cam Year 3 results: Cosmology from cosmic shear two-point correlation functions, Phys. Rev. D **108**, 123518 (2023).

[5] L. Secco, S. Samuroff, E. Krause *et al.*, Dark Energy Survey Year 3 results: Cosmology from cosmic shear and robustness to modeling uncertainty, Phys. Rev. D **105**, 023515 (2022).

[6] Planck Collaboration, Planck 2018 results VI. Cosmological parameters, Astron. Astrophys. **641**, A6(E) (2020).

[7] A. Amon and G. Efstathiou, A non-linear solution to the S8 tension? Mon. Not. R. Astron. Soc. **516**, 5355 (2022).

[8] T. Abbott, M. Aguena *et al.* (DES and KiDS Collaborations), DES Y3 + KiDS-1000: Consistent cosmology combining cosmic shear surveys, Open J. Astrophys. **6**, (2023).
[9] C. Lamman, E. Tsaprazi, J. Shi *et al.*, The IA guide: A breakdown of intrinsic alignment formalisms, arXiv: 2309.08605.
[10] M. Troxel and M. Ishak, The intrinsic alignment of galaxies and its impact on weak gravitational lensing in an era of precision cosmology, Phys. Rep. **558**, 1 (2015).
[11] L. Bigwood, A. Amon, A. Schneider *et al.*, Weak lensing combined with the kinetic Sunyaev–Zel'dovich effect: a study of baryonic feedback, Mon. Not. R. Astron. Soc. **534**, 655 (2024).
[12] Euclid Collaboration, Euclid preparation VII. Forecast validation for Euclid cosmological probes, Astron. Astrophys. **642**, A191 (2020).
[13] LSST Science Collaboration, LSST science book, version 2.0, arXiv:0912.0201.
[14] D. Spergel, N. Gehrels, C. Baltay *et al.*, Wide-field infrarred survey telescope-astrophysics focused telescope assets WFIRST-AFTA 2015 report, arXiv:1503.03757.
[15] R. Mandelbaum, T. Eifler *et al.* (LSST DESC Collaboration), The LSST Dark Energy Science Collaboration (DESC) Science Requirements Document (2018).
[16] S. Bridle and L. King, Dark energy constraints from cosmic shear power spectra: impact of intrinsic alignments on photometric redshift requirements, New J. Phys. **9**, 444 (2007).
[17] C. M. Hirata and U. Seljak, Intrinsic alignment-lensing interference as a contaminant of cosmic shear, Phys. Rev. D **70**, 063526 (2004).
[18] J. A. Blazek, N. MacCrann, M. Troxel, and X. Fang, Beyond linear galaxy alignments, Phys. Rev. D **100**, 103506 (2019).
[19] B. Joachimi, R. Mandelbaum, F. B. Abdalla, and S. L. Bridle, Constraints on intrinsic alignment contamination of weak lensing surveys using the MegaZ-LRG sample, Astron. Astrophys. **527**, A26 (2011).
[20] S. Samuroff, A. Campos, A. Porredon, and J. Blazek, Joint constraints from cosmic shear, galaxy-galaxy lensing and galaxy clustering: internal tension as an indicator of intrinsic alignment modelling error, Open J. Astrophys. **7**, 40 (2024).
[21] S. Samuroff, R. Mandelbaum, J. Blazek *et al.*, The Dark Energy Survey Year 3 and eBOSS: constraining galaxy intrinsic alignments across luminosity and colour space, Mon. Not. R. Astron. Soc. **524**, 2195 (2023).
[22] C. Lamman, D. Eisenstein, J. E. Forero-Romero *et al.*, Detection of the large-scale tidal field with galaxy multiplet alignment in the DESI Y1 spectroscopic survey, Mon. Not. R. Astron. Soc. **534**, 3540 (2024).
[23] M. C. Fortuna, H. Hoekstra, B. Joachimi *et al.*, The halo model as a versatile tool to predict intrinsic alignments, Mon. Not. R. Astron. Soc. **501**, 2983 (2020).
[24] T. Bakx, T. Kurita, N. Elisa Chisari, Z. Vlah, and F. Schmidt, Effective field theory of intrinsic alignments at one loop order: A comparison to dark matter simulations, J. Cosmol. Astropart. Phys. 10 (2023) 005.
[25] S.-F. Chen and N. Kokron, A Lagrangian theory for galaxy shape statistics, J. Cosmol. Astropart. Phys. 01 (2024) 027.
[26] J. Harnois-Déraps, N. Martinet, and R. Reischke, Cosmic shear beyond 2-point statistics: Accounting for galaxy intrinsic alignment with projected tidal fields, Mon. Not. R. Astron. Soc. **509**, 3868 (2022).
[27] K. Hoffmann, L. F. Secco, J. Blazek *et al.*, Modeling intrinsic galaxy alignment in the MICE simulation, Phys. Rev. D **106**, 123510 (2022).
[28] F. Maion, R. E. Angulo, T. Bakx, N. Elisa Chisari, T. Kurita, and M. Pellejero-Ibáñez, HYMALAIA: A hybrid lagrangian model for intrinsic alignments, Mon. Not. R. Astron. Soc. **531**, 2684 (2024).
[29] Z. Vlah, N. E. Chisari, and F. Schmidt, An EFT description of galaxy intrinsic alignments, J. Cosmol. Astropart. Phys. 01 (2020) 025.
[30] S. Chen, J. DeRose, R. Zhou *et al.*, Analysis of DESI × DES using the Lagrangian effective theory of LSS, Phys. Rev. D **110**, 103518 (2024).
[31] A. M. Delgado, B. Hadzhiyska, S. Bose *et al.*, The MillenniumTNG project: Intrinsic alignments of galaxies and haloes, Mon. Not. R. Astron. Soc. **523**, 5899 (2023).
[32] S. Samuroff, R. Mandelbaum, and J. Blazek, Advances in constraining intrinsic alignment models with hydrodynamic simulations, Mon. Not. R. Astron. Soc. **508**, 637 (2021).
[33] J. Blazek, M. McQuinn, and U. Seljak, Testing the tidal alignment model of galaxy intrinsic alignment, J. Cosmol. Astropart. Phys. 05 (2011) 010.
[34] C. M. Hirata, R. Mandelbaum, M. Ishak, U. Seljak , R. Nichol, K. A. Pimbblet, N. P. Ross, and D. Wake, Intrinsic galaxy alignments from the 2SLAQ and SDSS surveys: luminosity and redshift scalings and implications for weak lensing surveys, Mon. Not. R. Astron. Soc. **381**, 1197 (2007).
[35] M. C. Fortuna, H. Hoekstra, H. Johnston *et al.*, KiDS-1000: Constraints on the intrinsic alignment of luminous red galaxies, Astron. Astrophys. **654**, A76 (2021).
[36] H. Johnston, C. Georgiou, B. Joachimi *et al.*, KiDS +GAMA: Intrinsic alignment model constraints for current and future weak lensing cosmology, Astron. Astrophys. **624**, A30 (2019).
[37] R. Mandelbaum, C. Blake, S. Bridle *et al.*, The WiggleZ Dark Energy Survey: direct constraints on blue galaxy intrinsic alignments at intermediate redshifts, Mon. Not. R. Astron. Soc. **410**, 844 (2011).
[38] P. Catelan, M. Kamionkowski, and R. D. Blandford, Intrinsic and extrinsic galaxy alignment, Mon. Not. R. Astron. Soc. **320**, L7 (2001).
[39] J. Mackey, M. White, and M. Kamionkowski, Theoretical estimates of intrinsic galaxy alignment, Mon. Not. R. Astron. Soc. **332**, 788 (2002).
[40] S. Samuroff, J. Blazek, M. A. Troxel *et al.*, Dark Energy Survey Year 1 results: constraints on intrinsic alignments and their colour dependence from galaxy clustering and weak lensing, Mon. Not. R. Astron. Soc. **489**, 5453 (2019).
[41] C. Heymans, E. Grocutt, A. Heavens *et al.*, CFHTLenS tomographic weak lensing cosmological parameter constraints: Mitigating the impact of intrinsic galaxy alignments, Mon. Not. R. Astron. Soc. **432**, 2433 (2013).
[42] S.-S. Li, K. Kuijken, H. Hoekstra *et al.*, KiDS+VIKING-450: An internal-consistency test for cosmic shear tomography with a colour-based split of source galaxies, Astron. Astrophys. **646**, A175 (2021).

[43] E. Krause, T. Eifler, and J. Blazek, The impact of intrinsic alignment on current and future cosmic shear surveys, Mon. Not. R. Astron. Soc. **456**, 207 (2015).

[44] M. Gatti, E. Sheldon, A. Amon *et al.*, Dark energy survey year 3 results: Weak lensing shape catalogue, Mon. Not. R. Astron. Soc. **504**, 4312 (2021).

[45] J. Myles, A. Alarcon, A. Amon *et al.*, Dark Energy Survey Year 3 results: Redshift calibration of the weak lensing source galaxies, Mon. Not. R. Astron. Soc. **505**, 4249 (2021).

[46] W. G. Hartley, A. Choi, A. Amon *et al.*, Dark Energy Survey Year 3 Results: Deep Field optical + near-infrared images and catalogue, Mon. Not. R. Astron. Soc. **509**, 3547 (2021).

[47] S. Everett, B. Yanny, N. Kuropatkin *et al.*, Dark Energy Survey Year 3 Results: Measuring the survey transfer function with Balrog, Astrophys. J. Suppl. Ser. **258**, 15 (2022).

[48] N. MacCrann, M. R. Becker, J. McCullough *et al.*, Dark Energy Survey Y3 results: Blending shear and redshift biases in image simulations, Mon. Not. R. Astron. Soc. **509**, 3371 (2021).

[49] A. C. CarnallR. J. McLure, J. S. DunlopR. Davé, Inferring the star formation histories of massive quiescent galaxies with bagpipes: Evidence for multiple quenching mechanisms, Mon. Not. R. Astron. Soc. **480**, 4379 (2018).

[50] G. B. Brammer, P. G. van Dokkum, and P. Coppi, EAZY: A fast, public photometric redshift code, Astrophys. J. **686**, 1503 (2008).

[51] A. J. Mead, S. Brieden, T. Tröster, and C. Heymans, HMCODE-2020: Improved modelling of non-linear cosmological power spectra with baryonic feedback, Mon. Not. R. Astron. Soc. **502**, 1401 (2021).

[52] M. L. Brown, A. N. Taylor, N. C. Hambly, and S. Dye, Measurement of intrinsic alignments in galaxy ellipticities, Mon. Not. R. Astron. Soc. **333**, 501 (2002).

[53] M. A. Troxel, N. MacCrann, J. Zuntz *et al.*, Dark Energy Survey Year 1 results: Cosmological constraints from cosmic shear, Phys. Rev. D **98**, 043528 (2018).

[54] T. M. C. Abbott, M. Aguena, A. Alarcon *et al.*, Dark Energy Survey Year 3 results: Cosmological constraints from galaxy clustering and weak lensing, Phys. Rev. D **105**, 023520 (2022).

[55] G. Efstathiou and S. Gratton, A detailed description of the CAMSPEC likelihood pipeline and a reanalysis of the Planck high frequency maps, Open J. Astrophys. **4** (2021).

[56] M. Raveri and W. Hu, Concordance and discordance in cosmology, Phys. Rev. D **99**, 043506 (2019).

[57] C. García-García, M. Zennaro, G. Aricò, D. Alonso, and R. E. Angulo, Cosmic shear with small scales: DES-Y3, KiDS-1000 and HSC-DR1, J. Cosmol. Astropart. Phys. 08 (2024) 024.

[58] G. Aricò, R. E. Angulo, M. Zennaro *et al.*, DES Y3 cosmic shear down to small scales: Constraints on cosmology and baryons, Astron. Astrophys. **678**, A109 (2023).

[59] Ž. Ivezić, S. M. Kahn, J. A. Tyson *et al.*, LSST: From science drivers to reference design and anticipated data products, Astrophys. J. **873**, 111 (2019).

[60] Euclid Collaboration, I. The euclid wide survey, Astron. Astrophys. **662**, A112 (2022).

[61] R. Akeson, L. Armus, E. Bachelet *et al.*, The wide field infrared survey telescope: 100 Hubbles for the 2020s, arXiv:1902.05569.

[62] J. Siegel, J. McCullough, A. Amon *et al.*, Intrinsic alignment demographics for next-generation lensing: Revealing galaxy property trends with DESI Y1 direct measurements, arXiv:2507.11530.

[63] R. Buchs, C. Davis, D. Gruen *et al.*, Phenotypic redshifts with self-organizing maps: A novel method to characterize redshift distributions of source galaxies for weak lensing, Mon. Not. R. Astron. Soc. **489**, 820 (2019).

[64] O. Friedrich, F. Andrade-Oliveira, H. Camacho *et al.*, Dark Energy Survey year 3 results: Covariance modelling and its impact on parameter estimation and quality of fit, Mon. Not. R. Astron. Soc. **508**, 3125 (2021).

[65] X. Fang, T. Eifler, and E. Krause, 2D-FFTLog: Efficient computation of real-space covariance matrices for galaxy clustering and weak lensing, Mon. Not. R. Astron. Soc. **497**, 2699 (2020).

[66] A. Stebbins, Weak lensing on the celestial sphere, arXiv:astro-ph/9609149.

[67] M. LoVerde and N. Afshordi, Extended Limber approximation, Phys. Rev. D **78**, 123506 (2008).

[68] C. Howlett, A. Lewis, A. Hall, and A. Challinor, CMB power spectrum parameter degeneracies in the era of precision cosmology, J. Cosmol. Astropart. Phys. 04 (2012) 027.

[69] A. Lewis, A. Challinor, and A. Lasenby, Efficient computation of cosmic microwave background anisotropies in closed Friedmann-Robertson-Walker models, Astrophys. J. **538**, 473 (2000).

[70] J. E. McEwen, X. Fang, C. M. Hirata, and J. A. Blazek, FAST-PT: A novel algorithm to calculate convolution integrals in cosmological perturbation theory, J. Cosmol. Astropart. Phys. 09 (2016) 015.

[71] J. Zuntz, M. Paterno, E. Jennings *et al.*, CosmoSIS: Modular cosmological parameter estimation, Astron. Comput. **12**, 45 (2015).

[72] P. Lemos, N. Weaverdyck, R. P. Rollins *et al.*, Robust sampling for weak lensing and clustering analyses with the Dark Energy Survey, Mon. Not. R. Astron. Soc. **521**, 1184 (2023).

[73] W. J. Handley, M. P. Hobson, and A. N. Lasenby, POLYCHORD: Next-generation nested sampling, Mon. Not. R. Astron. Soc. **453**, 4385 (2015).

[74] W. J. Handley, M. P. Hobson, and A. N. Lasenby, POLYCHORD: Nested sampling for cosmology, Mon. Not. R. Astron. Soc.: Lett. **450**, L61 (2015).

[75] A. Lewis and A. Challinor, CAMB: Code for Anisotropies in the Microwave Background, Astrophysics Source Code Library, record ascl:1102.026 (2011).

[76] C. Patrignani, Review of particle physics, Chin. Phys. C **40**, 100001 (2016).

[77] B. Hadzhiyska, S. Ferraro, R. Pakmor *et al.*, Interpreting Sunyaev–Zel'dovich observations with MillenniumTNG: Mass and environment scaling relations, Mon. Not. R. Astron. Soc. **526**, 369 (2023).

[78] C. D. Leonard, M. M. Rau, and R. Mandelbaum, Photometric redshifts and intrinsic alignments: Degeneracies and biases in the 3 ×2×pt analysis, Phys. Rev. D **109**, 083528 (2024).

[79] J. McCullough, DES Y3: Blue Shear Datavector and Cosmology Chain [Data set] (2026), 10.5281/zenodo.18762855; https://jamiemccullough.github.io/data/blueshear/.